Geological Magazine

www.cambridge.org/geo

Original Article

Cite this article: Pundir S, Adlakha V, Kumar S, and Singhal S (2020) Closure of India–Asia collision margin along the Shyok Suture Zone in the eastern Karakoram: new geochemical and zircon U–Pb geochronological observations. *Geological Magazine* **157**: 1451–1472. https://doi.org/10.1017/S0016756819001547

Received: 23 May 2019
Revised: 17 December 2019
Accepted: 23 December 2019
First published online: 24 February 2020

Keywords:
magmatism; geochronology; Karakoram; Shyok Suture Zone

Author for correspondence:
Vikas Adlakha,
Email: vikas.himg@gmail.com

Closure of India–Asia collision margin along the Shyok Suture Zone in the eastern Karakoram: new geochemical and zircon U–Pb geochronological observations

Shailendra Pundir[1], Vikas Adlakha[1], Santosh Kumar[2] and Saurabh Singhal[1]

[1]Wadia Institute of Himalayan Geology, Dehradun, Uttarakhand, 248001, India and [2]Centre of Advanced Study, Department of Geology, Kumaun University, Nainital, Uttarakhand, 263001, India

Abstract

New whole-rock geochemical analyses along with laser ablation multi-collector inductively coupled plasma mass spectrometry U–Pb zircon ages of the granite–rhyolite from the Karakoram Batholith, exposed along the Shyok Valley, NW India, have been performed to understand the timing and geochemical evolution of these magmatic bodies and their implications for the geodynamic evolution of the Karakoram Batholith. New geochronological data on granites and rhyolites along with previously published geochronological data indicate that the Karakoram Batholith evolved during Albian time (~110–100 Ma) owing to the subduction of Tethys oceanic lithosphere along the Shyok Suture Zone. This region witnessed a period of no magmatism during ~99–85 Ma. Following this, the Kohistan–Ladakh arc and Karakoram Batholith evolved as a single entity in Late Cretaceous and early Palaeogene times. Late Cretaceous (~85 Ma) rhyolite intrusions within the Karakoram Batholith show calc-alkaline subduction-related signatures with a highly peraluminous nature (molar A/CNK = 1.42–1.81). These intrusions may have resulted from *c.* ~13.8 % to ~34.5 % assimilation of pre-existing granites accompanied by fractional crystallization during the ascent of the magma. The contamination of mantle wedge-derived melts with crust of the active continental margin of the Karakoram most likely enhanced the high peraluminous nature of the rhyolite magma, as has been constrained by assimilation fractional crystallization modelling. Two granite samples from the contact of the Shyok Metamorphic Complex and Karakoram Batholith indicate that the post-collisional Miocene magmatism was not only confined along the Karakoram Fault zone but also extends ~30 km beyond the Shyok–Muglib strand.

1. Introduction

Active continental margins record the evolutionary history of subduction-related magmatic events (Murphy, 2006; Xiao *et al.* 2016; Lallemand & Heuret, 2017) and can be considered the central region of continental crustal growth (Franz *et al.* 2006; Vogt *et al.* 2012) in continental collision zones. The Karakoram terrane forms the southern margin of the Asian plate (Jain & Singh, 2008; Searle & Hacker, 2018), which has witnessed periodic episodes of continental arc magmatism since Early Cretaceous time (Weinberg *et al.* 2000; Fraser *et al.* 2001; Heuberger *et al.* 2007; Upadhyay, 2008; Jain & Singh, 2009; Ravikant *et al.* 2009; Kumar *et al.* 2017). The accretion of the Karakoram with Asia was the result of the separation and northward drifting of the Karakoram from Gondwana that occurred during Permian time (Boulin, 1981; Tapponnier *et al.* 1981). Further, the closure of the Tethys ocean between the Indian and Asian plates along two suture zones, the Indus Tsangpo Suture Zone (ITSZ) in the south and Shyok Suture Zone (SSZ)/Main Karakoram Thrust (MKT) in the north, led to the formation of magmatic arcs during Mesozoic–early Tertiary times (Fig. 1a) (Windley, 1988; Jain & Singh, 2008).

A significant amount of data have been published to constrain the magmatic evolution of the Ladakh and Karakoram regions, which has helped to understand the geodynamic evolution of the India–Asia collision zone (e.g. Searle *et al.* 1987; Klootwijk *et al.* 1992; Rowley, 1996; Najman *et al.* 2010; Hu *et al.* 2016). However, the timing of suturing along the SSZ is still not well constrained as the existing chronological data provide a wide bracket ranging from ~110 Ma to ~75 Ma for the suturing event (Petterson & Windley, 1985; Treloar *et al.* 1996; Rolland *et al.* 2000; Heuberger *et al.* 2007; Ravikant *et al.* 2009; Borneman *et al.* 2015; Kumar *et al.* 2017). In this paper, we present new whole-rock geochemical data along with laser ablation multi-collector inductively coupled plasma mass spectrometry (LA-MC-ICP-MS) zircon U–Pb ages on the rhyolite and granites exposed in an unexplored remote region of the Karakoram Batholith that crops out along the upper Shyok Valley. The present paper provides a viable model for the

CAMBRIDGE UNIVERSITY PRESS

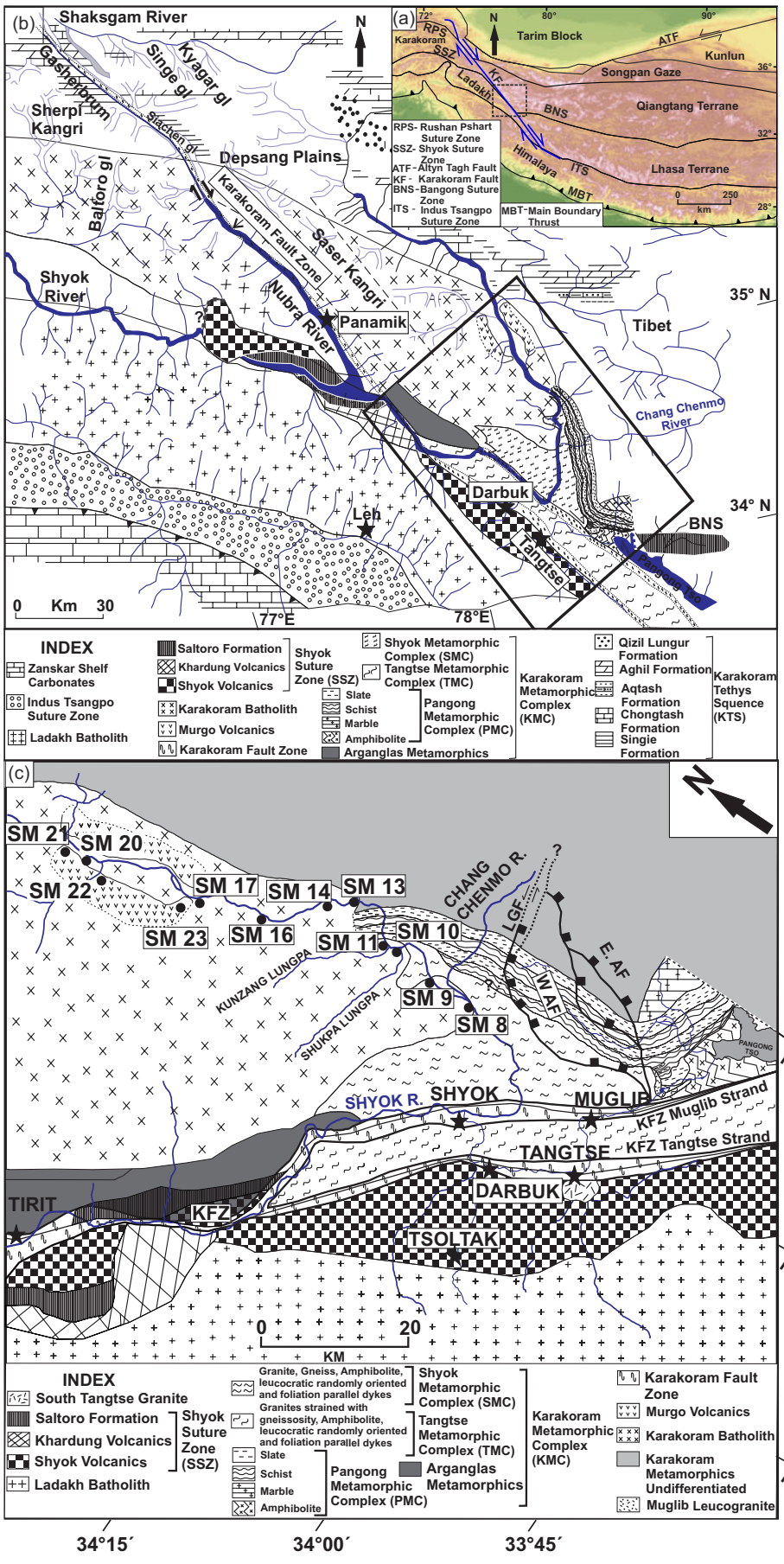

Fig. 1. (Colour online) Overview map of the Himalayan–Tibetan orogenic belt and geologic map across the Karakoram and Ladakh. (a) Map showing the main tectonic structures and sutures in the Himalaya, Tibet and the Karakoram region. (b) Simplified map showing the regional geology of the eastern Karakoram region (after Phillips, 2008) with the location of the study area in the rectangle. (c) Geological map of the SE Karakoram with the locations of collected samples from the Karakoram Batholith. The Longmu–Ghoza Co fault (LGF) and Angmong fault (AF) are from van Buer *et al.* (2015) (modified after Phillips *et al.* 2004; Jain & Singh 2008; Ravikant *et al.* 2009). (Sample location SM 9 includes both SM 9A and SM 9B).

https://doi.org/10.1017/S0016756819001547 Published online by Cambridge University Press

timing and process of suturing along the SSZ. The fundamental basis for our proposed model is the evolution of rhyolite as a result of assimilation fractional crystallization (AFC), i.e. fractional crystallization of calc-alkaline subduction-derived melt accompanying the assimilation of thickened Asian continental margin in the Karakoram basement owing to the collision of the Kohistan–Ladakh arc (KLA) orogen (for example, Manikyamba *et al.* 2014).

2. Background

2.a. Geological setting

The Karakoram terrane juxtaposes the SSZ on its southern margins (Coward *et al.* 1982, 1986; Pudsey *et al.* 1985) and the Rushan–Pshart Suture (RPS) zone to the north (Shvolman, 1978; Rex *et al.* 1988) (Fig. 1a, b). This terrane can be divided from south to north into four litho-domains, viz. (a) the Karakoram Fault Zone (KFZ); (b) the Karakoram Metamorphic Complex (KMC), which includes the Shyok Metamorphic Complex (SMC), Tangtse Metamorphic Complex (TMC), Pangong Metamorphic Complex (PMC) and Arganglas Metamorphics; (c) the Karakoram Batholith (KB); and (d) the Karakoram Tethys Sequence (KTS) (Rai, 1995; Searle *et al.* 1998; Jain & Singh, 2008) (Fig. 1b, c).

The KFZ is characterized by the presence of ductile deformed rocks in the north of the SSZ that formed as a result of dextral deformation along the Karakoram Fault (KF). In the eastern Karakoram region, the KF passes through the Nubra Valley (Fig. 1b, c) with a major restraining bend that splays into two strands, viz. the Tangtse strand and Muglib strand, as shown in Figure 1c. The Tangtse strand passes through Darbuk and Tangtse villages, while the Muglib strand passes through Shyok and Muglib villages (Fig. 1c). These two strands bound a transpressional uplifted metamorphic complex that is mainly dominated by high-grade metamorphic rocks intruded by foliation-parallel and cross-cutting leucocratic dykes (Searle *et al.* 1998; Phillips *et al.* 2004; Rolland *et al.* 2009; Boutonnet *et al.* 2012). The KF exposes well-deformed rocks in a ~1–8 km wide zone that mainly comprise mylonitic granite gneiss with steep vertical foliations, having nearly horizontal stretching lineations (Figs 1c, 2a–c). The KFZ is primarily composed of mylonitic granite gneiss, volcanic rocks, slate, phyllite and amphibolite (e.g. Boutonnet *et al.* 2012; Sen *et al.* 2014). The ductile deformation along the KF in this region was initiated at ~23 Ma or probably during ~18–15 Ma (Weinberg *et al.* 2000; Phillips *et al.* 2004; Boutonnet *et al.* 2012). Tectono-metamorphic studies (Rolland & Pêcher, 2001), teleseismic studies using receiver functions (Hazarika *et al.* 2014; Hazarika *et al.* 2017) and He-isotopic investigations in geothermal springs (Klemperer *et al.* 2013) suggest the nature of the KF as lithospheric.

The KMC extends all along the southern margin of the Asian plate and provides records of pre- to post India–Asia collisional high-grade metamorphic rocks (e.g. ~108 Ma: Streule *et al.* 2009; ~32–8 Ma: Rolland *et al.* 2009; Boutonnet *et al.* 2012). Pre- to syn-collisional metamorphism has been reported from the western Karakoram (e.g. from the Hunza region) (Fraser *et al.* 2001) and the Pangong region of the eastern Karakoram as well (Rolland *et al.* 2009; Streule *et al.* 2009; Wallis *et al.* 2014). This metamorphism has been attributed to pre-collisional magmatism, the accretion of the KLA with the Asian plate, and the subsequent collision of India and Asia (Fraser *et al.* 2001; Rolland *et al.* 2009; Streule *et al.* 2009; Wallis *et al.* 2014). However, the post-collisional metamorphism has been attributed either to ductile deformation along the KF that has exposed greenschist- to granulite-grade metamorphic rocks along the KFZ (e.g. Weinberg *et al.* 2009; Rolland *et al.* 2009) or to compression and crustal thickening led by India–Asia continental collision (Searle *et al.* 1998; Phillips *et al.* 2004; Phillips & Searle, 2007; Searle & Phillips, 2007).

In the eastern Karakoram, the highly metamorphosed and migmatized rocks of the KMC are best exposed near the Darbuk, Shyok and Tangtse regions of Ladakh, NW India (Fig. 1c). The Tangtse and Muglib strands of the KF bound the TMC or Pangong Injection Complex (PIC) (Figs 1c, 2d) (Weinberg & Searle, 1998; Jain & Singh, 2008). The TMC mainly consists of high-grade metamorphic rocks such as amphibolites, orthogneisses and migmatites that are intruded by several foliation-parallel and cross-cutting leucogranite-pegmatite dykes (Searle *et al.* 1998; Phillips *et al.* 2004; Rolland *et al.* 2009; Boutonnet *et al.* 2012). The age of metamorphism in this region has been reported to be 32–11 Ma (Rolland *et al.* 2009). Similar high-grade metamorphic rocks have also been observed in the present study even to the north of the Shyok–Muglib strand of the KF, upstream along the Shyok Valley, and referred to herein as the SMC (Figs 1c, 2e, f). The KF system forms a junction with the left-lateral Longmu–Ghoza Co fault in the region of the SMC (Fig. 1c). This intersection has resulted in the formation of an extensional detachment system (Fig. 1c) (van Buer *et al.* 2015; Bohon *et al.* 2018). One can observe the extensional and strike-slip deformation-related features of these fault systems in the field only within a narrow zone of 5–10 km in the vicinity of the Muglib strand of the KF (Figs 1c, 2g). Medium-to-low-grade metamorphic rocks that mainly consist of schists, slates, marble and amphibolites are exposed to the northeast of the Muglib strand and are locally named the PMC, which forms part of the KMC (Fig. 1c). These rocks are well exposed near the Pangong Tso region in the Tangtse Valley (Figs 1c, 2h) and as thin patches in the Shyok Valley upstream (Fig. 3a).

The KB that forms the litho-unit to the north of the KMC (Fig. 1b) extends from northern Pakistan to southwestern Tibet through the Ladakh region of the eastern Karakoram, India (Rai, 1995). Two types of granites, metaluminous (I-type) and peraluminous (S-type) granites (Chappell & White, 1974), have been reported from the KB, and intrude the Karakoram Tethyan Zone (Srimal *et al.* 1987; Rai, 1995; Jain & Singh, 2008; Ravikant *et al.* 2009). The pre-collisional I-type suite comprises mainly quartz monzonite, granodiorite and tonalite, while the post-collisional S-type suite is composed mainly of two-mica leucogranites (Phillips *et al.* 2004; Ravikant, 2006; Jain & Singh, 2008; Leloup *et al.* 2011).

The unexplored undeformed region of the KB lying to the north of the SMC and PMC forms the site of the present investigation (Fig. 1c). The intrusive contact of the KB with the SMC (Fig. 3b) and PMC is sharp (Fig. 3a). The KB is mainly composed of massive porphyritic granites that are devoid of any foliation or lineations (Figs 1c, 3c, d), unlike the rocks of the TMC and SMC, which are strongly foliated (Fig. 2b, f). Field relationships indicate that the northern (undeformed) domain of the KB did not experience metamorphism or deformation during the collisional or post-collisional regimes (Fig. 3c, d). Modally, the granitoids range in composition from granite to granodiorite. Texturally, the porphyritic granites of the KB consist of randomly oriented ~2–5 cm long plagioclase and K-feldspar crystals embedded in a fine-grained felsic matrix (Fig. 3c). The undeformed extrusive felsic volcanic rocks (rhyolite), referred to herein as the Murgo Volcanics (MV), can be observed exposed within the KB

https://doi.org/10.1017/S0016756819001547 Published online by Cambridge University Press

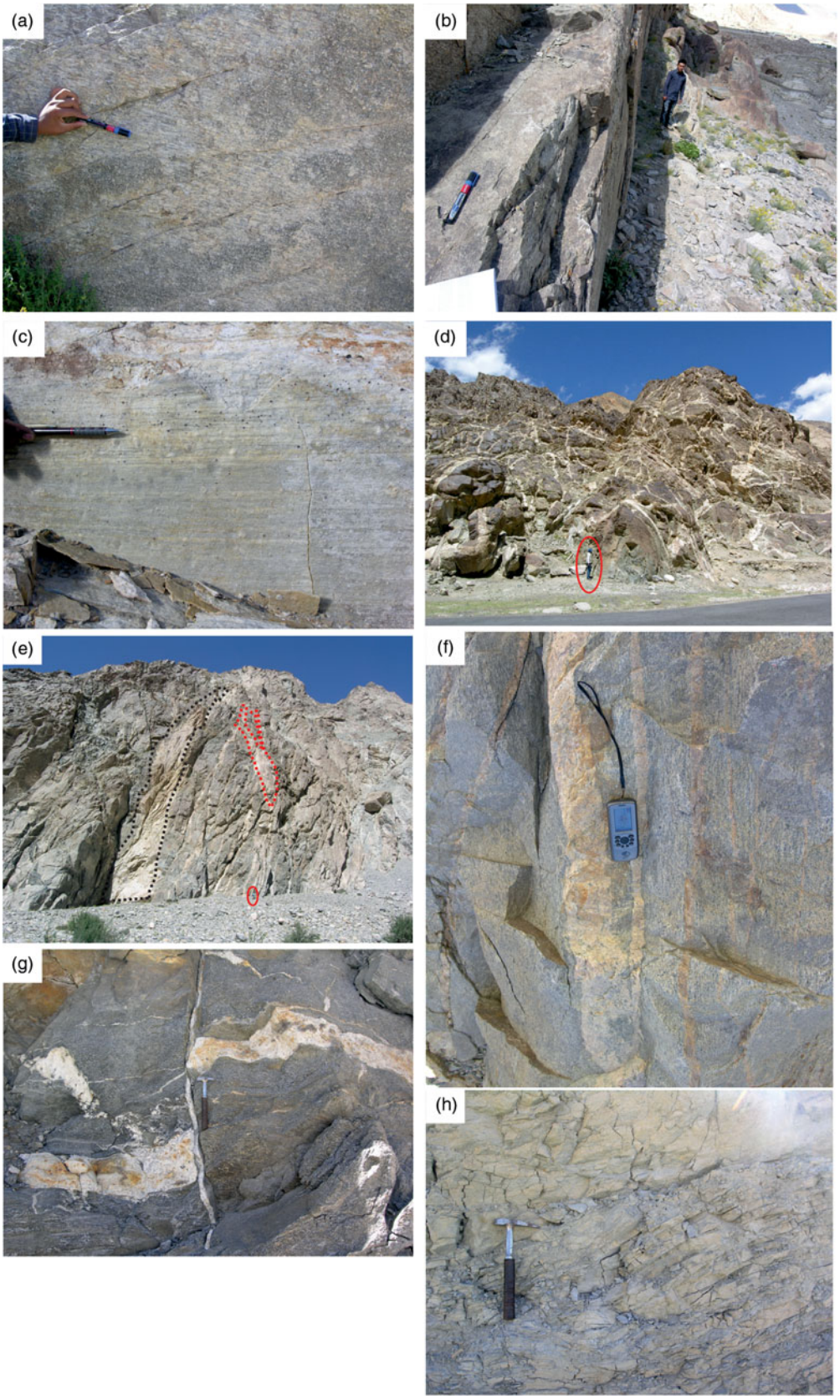

Fig. 2. (Colour online) Outcrop-scale structures from the KFZ and upstream Shyok Valley. (a) Horizontal lineations representing the Tangtse strand of the KFZ. (b) Vertical foliation near the Tangtse strand of the KFZ. (c) Horizontal lineations representing the Muglib strand of the KFZ. Pen for scale is ~ 13 cm long. (d) Migmatization in the TMC of the KFZ. (e) Foliation-parallel (black) and cross-cutting (red) leucocratic dyke intrusions within the SMC. (f) Leucocratic dyke intrusions parallel to the foliation plane within the SMC. GPS for scale is ~30 cm long. (g) Normal faulting showing extensional feature in the north of the Shyok–Muglib strand. (h) Well-exposed marble near the Pangong Tso region in the Tangtse Valley. Geological hammer for scale is ~33 cm long.

(Figs 1c, 3e, f). The contact of the rhyolite with the granite is poorly exposed and not assessed owing to inaccessible topography and debris cover. However, it appears that the rhyolite rests over the regionally exposed KB (Fig. 3f). Texturally, the rhyolite is mainly aphanitic and consists of tiny (up to 1 mm long) crystals of quartz and K-feldspar.

The rocks of the KB are in juxtaposition with the KTS of Permo-Carboniferous to Middle Jurassic age to the north. This block of the

https://doi.org/10.1017/S0016756819001547 Published online by Cambridge University Press

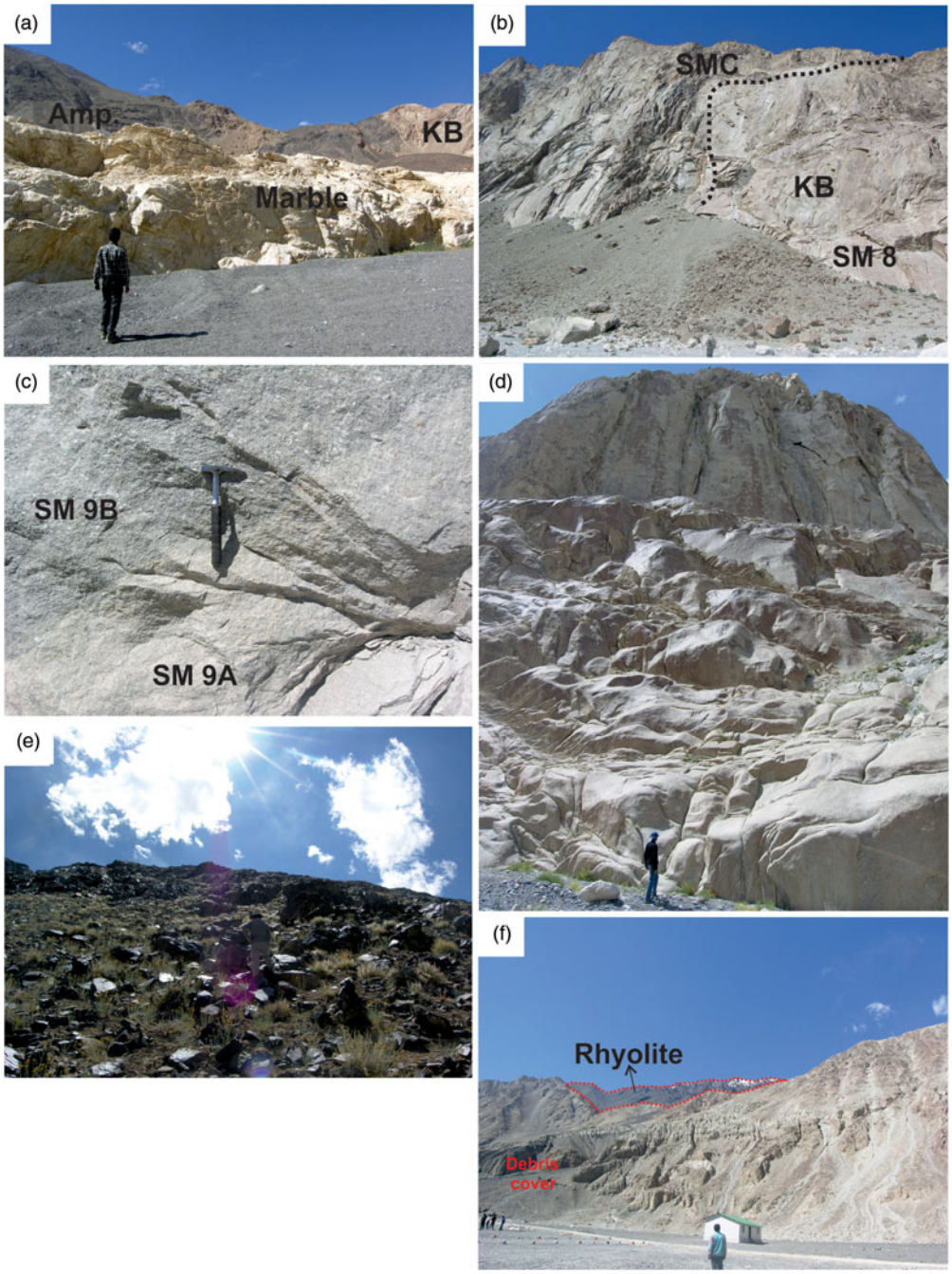

Fig. 3. (Colour online) Outcrop-scale structures from the upstream Shyok Valley. (a) Marble and amphibolite schist of the PMC mapped along the Shyok river in the NE of the Shyok–Muglib strand of the KF. (b) Contact of the SMC with the KB. (c) Porphyritic granites with large laths of K-feldspar and plagioclase feldspar. Geological hammer for scale is ~33 cm long. (d) Undeformed granite body of the KB. (e, f) Contact of the Murgo Volcanics (rhyolites) with the KB.

Karakoram terrane is equivalent to the Qiangtang Block of Tibet (Fig. 1b) (Searle, 2015). The KTS consists of limestone, shale, slate, sandstone and quartzite to the north of the KB along the upper Shyok Valley (Gergan & Pant, 1983) (Fig. 1b), but the burial and exhumation history of these sediments is still unknown.

2.b. Previous geochronological record

The SSZ represents the region of the initial subduction phase of the Neo-Tethyan oceanic lithosphere beneath the southern margin of the Asian plate (Crawford & Searle, 1992; Searle *et al.* 1998; Heuberger *et al.* 2007; Kumar *et al.* 2017). The subduction of Neo-Tethyan oceanic lithosphere produced the large-scale NW–SE-striking KB, which mainly comprises pre-collisional subduction-related calc-alkaline granites emplaced during Cretaceous time or earlier (Fig. 1c) (Debon *et al.* 1987; Crawford & Searle, 1992; Searle *et al.* 1998; Heuberger *et al.* 2007; Kumar *et al.* 2017). In the NW region of the Karakoram, these granites include the Hunza plutonic unit (~105 Ma; Fraser *et al.* 2001), K2 gneiss (~120–115 Ma; Searle *et al.* 1990), Tirich Mir granite (~121–115 Ma; Desio *et al.* 1964; Heuberger *et al.* 2007), Muztag Tower unit (~82 Ma; Searle *et al.* 1988) and Hushe gneiss (~145 Ma; Searle *et al.* 1989). In the eastern Karakoram, these are recognized as the Tirit granites (~110–68 Ma; Weinberg *et al.* 2000; Jain & Singh, 2008; Upadhyay, 2008; Kumar *et al.* 2017) and Panamik granite in the Khalsar–Panamik region (~105 Ma) (Rao & Rai, 2009; Ravikant *et al.* 2009) exposed in the Nubra Valley, Ladakh region of NW India (Fig. 1c).

https://doi.org/10.1017/S0016756819001547 Published online by Cambridge University Press

The SSZ exposes calc-alkaline volcanic rocks in the Khardung and Shyok formations in the Ladakh region (Thakur *et al.* 1981; Srimal *et al.* 1987; Dunlap & Wysoczanski, 2002; Borneman *et al.* 2015) (Fig. 1c). The Khardung Formation includes felsic and intermediate volcanic rocks, tuffs and sediments (Thakur *et al.* 1981; Srimal *et al.* 1987; Kumar *et al.* 2016). Geochemically, the Khardung Volcanics are calc-alkaline and are considered to be the volcanic counterpart of the Ladakh Batholith (Srimal *et al.* 1987; Weinberg & Dunlap, 2000; Thanh *et al.* 2010; Kumar *et al.* 2017). Dunlap & Wysoczanski (2002) reported a zircon U–Pb age of ~67 Ma for the rhyolite and an intrusion age of ~60 Ma for a porphyritic sill from the Khardung Volcanics, defining Late Cretaceous – early Tertiary ages for the eruption of the volcanic rocks. The Shyok Formation includes sediments and volcanic mafic to ultramafic rocks (Thakur *et al.* 1981). The minimum age of volcanism in the Shyok Formation has been reported to be ~125 Ma, based on an ^{40}Ar–^{39}Ar hornblende age from a hypabyssal dyke from the eastern Karakoram (Borneman *et al.* 2015), and older than *c.* 110 Ma, inferred from the intrusive relationship of the Tirit granites (*c.* 110–104 Ma) with the Shyok Volcanics (Kumar *et al.* 2017).

Records of post-India–Asia collision-related two-mica (S-type) granites within the KB have also been found, which were emplaced during Miocene time as a result of either crustal rejuvenation due to compressional heating or dextral shearing along the KF (Searle *et al.* 1989; Phillips *et al.* 2004; Ravikant, 2006; Boutonnet *et al.* 2012). The two-mica (S-type) granites extend from the NW to SE regions of the Karakoram, and include the Baltoro plutonic unit (~21 Ma; Searle *et al.* 1988; Parrish & Tirrul, 1989; Fraser *et al.* 2001) and leucogranite intrusions within the TMC (21–14 Ma; Searle *et al.* 1998; Phillips *et al.* 2004; Jain & Singh, 2008; Ravikant *et al.* 2009; Reichardt *et al.* 2010; Leloup *et al.* 2011; Phillips *et al.* 2013; Sen *et al.* 2014). These two-mica granites and leucogranites are considered to be of crustal origin.

2.c. Sample selections as per field relationships

We collected ten samples of granite and three samples of rhyolite based on observed field relationships between the SMC and the KB. The granite samples SM 8 and SM 9A/B were collected from the SMC and KB contact (Figs 1c, 3a). These samples may preserve the features of partial melting within the SMC in the form of dissolution, overgrowth or recrystallization of zircon that can lead to perturbation, and possibly the resetting of zircon, which can constrain the thermal events that operated in this region. The remaining seven granite samples (SM 10, SM 11, SM 13, SM 14, SM 16, SM 17 and SM 20) along with the three rhyolite samples (SM 21, SM 22 and SM 23) were collected from further north along the upper Shyok Valley region (Fig. 1c) where the effect of partial melting within the SMC becomes negligible. The sample locations with coordinates are given in online Supplementary Material Table S1.

3. Methodology

Whole-rock geochemical analysis was carried out on ten granite (SM 8, SM 9A, SM 9B, SM 10, SM 11, SM 13, SM 14, SM 16, SM 17, SM 20) and three rhyolite (SM 21, SM 22, SM 23) samples, the locations of which are shown in Figure 1c. The samples were crushed using a jaw crusher and then powdered in an agate mill to sizes <200 mesh. Whole-rock major and trace elements were determined using wavelength dispersive X-ray fluorescence (WD-XRF) (Bruker S8 Tiger) on pressed-powder pellets at the Wadia Institute of Himalayan Geology (WIHG), Dehradun, India.

The methodology adopted in this paper is similar to that described by Singhal *et al.* (2019). The accuracy (% RDS) and precision of the results for major oxides are within 5 % and 1.5 %, respectively (Saini, 1998). The geochemical data processing and plotting were carried out using Geochemical Data Toolkit (Janoušek *et al.* 2006).

The rare earth element (REE) concentrations were measured using ICP-MS (Perkin-Elmer SCIEX ELAN DRC-e) at WIHG, Dehradun. We used an open-system digestion method to prepare the samples. A sample of 0.1 g of rock powder was mixed with (2:1) $HF + HNO_3$ solution of 20 ml in Teflon™ crucibles for the complete digestion of the sample. The digested samples were then extracted using 20 % HNO_3 and diluted to 100 ml volume. We used rock standards (JG-2 and MB-H) for calibration.

The zircon separates were obtained using conventional heavy liquid separation techniques. The zircon mounts were polished up to 0.25 micron using a diamond lapping compound. Backscattered electron (BSE) and cathodoluminescence (CL) images were taken using a scanning electron microscope (SEM-Zeiss EVO 40 EP) using Zeiss Everhart-Thornley SE and Chroma UV CL2 detectors. Zircon U–Pb ages were measured using an LA-MC-ICP-MS Neptune plus instrument (Thermofisher Scientific) coupled with an Analyte G2 193 nm ArF excimer laser ablation system (Teledyne) at WIHG, Dehradun, India. Zircon standard Harvard 91500 (TIMS reference age 1062.4 ± 0.4 Ma) (Wiedenbeck *et al.* 1995) was used as a primary standard for correcting the instrumental mass bias and downhole fractionation. However, we used Plesovice (TIMS reference age 337.13 ± 0.37 Ma) (Sláma *et al.* 2008) as a secondary standard for U–Pb geochronology. The complete methodology adopted in this paper is similar to that described by Mukherjee *et al.* (2017). Off-line processing of the data obtained from the mass spectrometer was done using Iolite version 2.5 (Paton *et al.* 2011). Concordia and histogram plotting was carried out using IsoplotR (Vermeesch, 2018). We used histograms to demonstrate and identify the peaks of the analysed zircon spots. We selected the highest peak to calculate the weighted mean age of the studied samples. We used IsoplotR (Vermeesch, 2018) for the calculation of weighted mean ages, which accounts for the analytical uncertainties in heteroscedastic datasets. IsoplotR provides three different calculated uncertainties with lower to upper bounds. We considered the upper uncertainty bound to exclude any error.

4. Petrography and geochemistry

The studied undeformed granites (SM 8, SM 9A, SM 9B, SM 10, SM 11, SM 13, SM 14, SM 16, SM 17, SM 20) of the pluton from the KB are medium to coarse grained, equigranular to porphyritic in nature, and mainly consist of quartz (Qz), K-feldspar (Kfs), plagioclase (Pl) and biotite (Bt) as the major rock-forming minerals (mineral symbols after Whitney & Evans, 2010) (Fig. 4a–i). The granites SM 9A and SM 9B are porphyritic with phenocrysts of K-feldspar and plagioclase (Fig. 4b, c). Hornblende (Hbl) can be observed only in one sample, SM 11 (Fig. 4e), while in all other samples, biotite is the mafic phase (Fig. 4a–i). Extrusive rhyolites (SM 21, SM 22, SM 23) that rest on the granite pluton (Fig. 3f) exhibit a porphyritic texture in which euhedral phenocrysts of sanidine (Sa), plagioclase and quartz are embedded within a felsic groundmass mainly composed of fine crystals of quartz, orthoclase and plagioclase. Features such as flow structures are not apparent,

https://doi.org/10.1017/S0016756819001547 Published online by Cambridge University Press

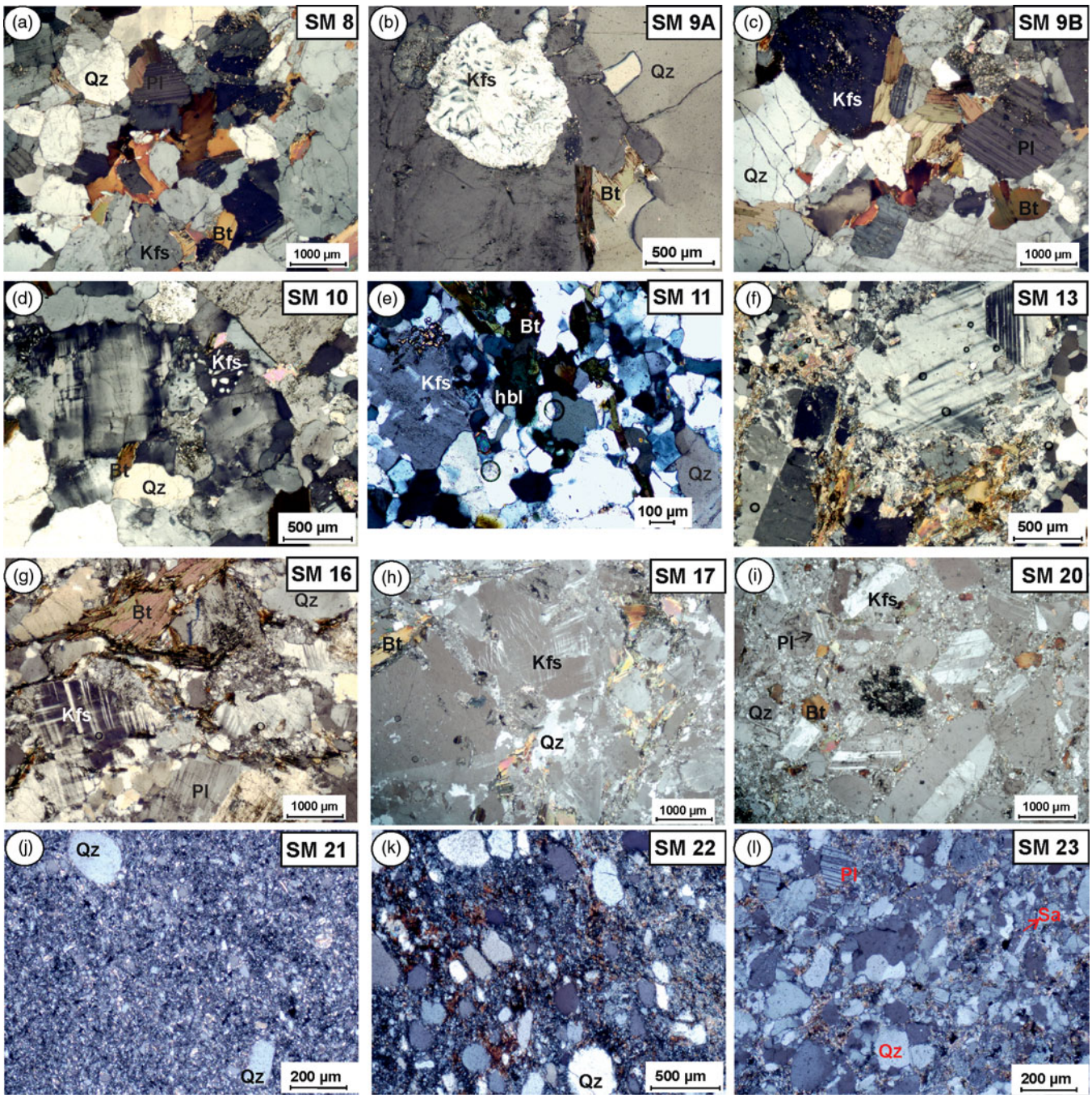

Fig. 4. (Colour online) Photomicrographs of the studied rock samples from the SMC and KB. (a–i) Granites showing medium- to coarse-grained porphyritic texture with phenocrysts of quartz (Qz), K-feldspar (Kfs), plagioclase (Pl) and biotite (Bt). (j–l) Porphyritic texture and exhibition of euhedral phenocrysts of sanidine (Sa), plagioclase and quartz. hbl – hornblende.

but phenocrysts of quartz and K-feldspar are present in the quenched glassy groundmass (Fig. 4j–l).

Table 1 presents the results of the whole-rock geochemical analysis. All granites exhibit a relatively wide range of SiO_2 (66.92–73.85 wt %) and K_2O (2.48–5.33 wt %) contents, belonging to the medium to high potassium calc-alkaline series (Fig. 5) (Peccerillo & Taylor, 1976). The granites are largely peraluminous, except the metaluminous granite samples SM 8 and SM 11; the A/CNK (molar $Al_2O_3/CaO + Na_2O + K_2O$, i.e. alumina saturation index of Shand, 1947) ratios range from 0.95 to 1.14. The rhyolites (SM 21, SM 22, SM 23) are strongly peraluminous (A/CNK = 1.42–1.81) (Fig. 6a). The nature of the differentiation series of silicic magma can be determined through $(FeO^t)/(FeO^t + MgO)$ (Frost *et al.* 2001), while the modified alkali lime index (Peacock, 1931) of a silicic magmatic suite can be used to decipher the nature and source of the magma (Frost *et al.* 2001). The granites and rhyolites follow the calc-alkali series, being magnesian (Fig. 6b, c). On the A/CNK versus SiO_2 plot (Chappell & White, 1974), the granites show I-type affinity, while the rhyolites lie in the S-type granite field (Fig. 6d). The granites and rhyolites do not show much compositional difference, plotting in the field of granite and granodiorite in terms of Na_2O versus SiO_2 (Middlemost, 1994)

https://doi.org/10.1017/S0016756819001547 Published online by Cambridge University Press

Table 1. Major- (wt %) and trace-element (ppm) contents of the analysed samples from the Karakoram Batholith, eastern Karakoram, India

Elements	SM 8	SM 9A	SM 9B	SM 10	SM 11	SM 13	SM14	SM 16	SM 17	SM 20	SM 21	SM 22	SM 23
SiO_2	70.15	73.85	66.92	72.29	70.53	67.63	70.70	72.08	67.13	67.80	65.88	71.16	71.49
TiO_2	0.29	0.08	0.45	0.21	0.40	0.51	0.18	0.30	0.48	0.54	0.95	0.68	0.71
Al_2O_3	15.24	14.92	16.74	14.27	13.63	14.48	15.61	14.18	15.59	14.86	16.74	13.07	14.37
$Fe_2O_3^t$	1.85	0.36	2.94	1.38	3.35	3.96	1.28	2.49	3.23	3.37	6.04	5.06	4.67
MnO	0.02	0.01	0.04	0.02	0.05	0.05	0.03	0.05	0.05	0.05	0.06	0.05	0.02
MgO	0.49	0.10	0.75	0.27	1.34	1.50	0.26	0.68	1.21	1.56	1.83	1.77	1.02
CaO	3.01	1.37	2.39	1.95	2.60	2.32	1.88	2.10	2.87	3.13	0.78	1.10	0.58
Na_2O	4.02	3.63	4.62	3.82	2.84	2.62	4.26	2.94	3.07	2.78	2.90	2.51	2.19
K_2O	2.93	5.33	2.48	4.06	4.48	4.80	3.76	4.35	4.05	4.01	3.37	2.83	3.03
P_2O_5	0.14	0.09	0.05	0.10	0.12	0.18	0.05	0.11	0.17	0.19	0.14	0.15	0.06
LOI	4.02	0.49	0.78	0.92	0.58	1.97	1.01	1.25	1.44	0.97	2.01	1.51	1.97
TOTAL	102.16	100.23	98.16	99.29	99.92	100.02	99.02	100.53	99.29	99.26	100.70	99.89	100.11
A/CNK	0.99	1.04	1.14	1.00	0.95	1.05	1.07	1.06	1.06	1.01	1.70	1.42	1.81
Sc	4.3	2.6	6.2	3.4	6.5	7.4	3.0	5.0	7.2	7.2	12.2	7.7	8.2
V	21	4	36	18	54	62	11	31	48	58	122	88	82
Ni	1	BDL	1	2	9	10	BDL	5	5	4	31	24	10
Cu	3	1	6	6	4	5	1	1	4	8	17	19	9
Zn	40	14	57	28	40	55	33	40	47	41	66	60	36
Ga	18	16	21	16	15	16	17	17	17	18	18	14	13
Pb	28	39	25	43	38	37	40	38	29	20	24	15	8
Th	8	5	47	21	51	44	19	22	18	19	10	9	7
Rb	95	117	104	123	236	240	122	200	172	138	118	94	104
U	BDL	BDL	4.3	3.0	5.6	4.0	BDL	5.0	4.8	5.5	2.4	BDL	BDL
Sr	528	253	395	443	226	308	457	245	309	517	163	120	114
Y	14	15	14	17	33	31	16	32	26	21	23	19	19
Zr	162	76	209	160	192	205	129	140	161	211	241	202	298
Nb	7	1	11	4	22	17	6	17	16	15	19	15	15
Ba	1084	302	614	930	436	618	1385	434	595	798	742	500	582
La	20.830	12.133	69.947	33.500	58.640	86.700	13.227	39.160	35.405	42.954	35.495	27.288	24.472
Ce	39.486	23.757	139.21	62.020	111.130	155.400	23.513	74.880	68.658	79.003	73.506	56.765	50.949
Pr	3.941	2.456	15.018	6.790	11.160	16.400	2.241	8.270	7.186	8.137	8.072	6.166	5.539
Nd	14.689	9.029	56.334	23.40	39.776	53.000	7.997	28.11	27.63	31.017	32.347	24.644	22.142
Sm	2.374	1.585	8.869	3.930	6.377	8.940	1.147	5.980	4.878	5.012	5.614	4.368	3.933
Eu	0.639	0.476	0.579	0.790	0.923	1.360	0.342	0.960	1.027	1.237	1.249	0.921	0.917
Gd	1.670	1.043	5.549	3.600	4.792	8.380	0.831	5.940	3.609	3.629	3.992	3.158	2.828
Tb	0.231	0.140	0.588	0.420	0.706	1.020	0.102	0.910	0.578	0.514	0.579	0.472	0.41
Dy	1.288	0.744	2.390	1.760	4.551	5.000	0.568	4.880	3.806	3.118	3.558	2.821	2.525
Ho	0.119	0.066	0.168	0.300	0.500	0.940	0.053	0.960	0.408	0.315	0.354	0.287	0.248
Er	0.354	0.204	0.471	0.760	1.745	2.670	0.167	2.520	1.383	1.026	1.153	0.920	0.780
Tm	0.036	0.022	0.032	0.080	0.233	0.380	0.020	0.380	0.181	0.122	0.140	0.110	0.094
Yb	0.320	0.207	0.275	0.530	2.374	2.560	0.192	2.500	1.902	1.234	1.429	1.079	0.953
Lu	0.047	0.031	0.041	0.070	0.384	0.380	0.033	0.360	0.311	0.191	0.235	0.171	0.153
∑REE	86.021	51.893	299.470	137.950	243.290	343.130	50.433	175.810	156.960	177.500	167.720	129.170	115.943

(*Continued*)

https://doi.org/10.1017/S0016756819001547 Published online by Cambridge University Press

Table 1. (*Continued*)

Elements	SM 8	SM 9A	SM 9B	SM 10	SM 11	SM 13	SM14	SM 16	SM 17	SM 20	SM 21	SM 22	SM 23
Rb/Sr	0.179	0.462	0.263	0.277	1.044	0.779	0.266	0.816	0.5566	0.266	0.723	0.783	0.912
La_N/Lu_N	46.00	40.63	177.11	49.68	15.85	23.69	41.61	11.29	11.82	23.35	15.68	16.57	16.60
Eu_N/Eu^*	0.98	1.13	0.25	0.64	0.51	0.48	1.07	0.49	0.74	0.88	0.80	0.75	0.84
La_N/Sm_N	5.52	4.82	4.96	5.37	5.79	6.10	7.26	4.12	4.57	5.39	3.98	3.93	3.92
Gd_N/Lu_N	4.42	4.19	16.85	6.40	1.55	2.75	3.14	2.05	1.44	2.37	2.12	2.30	2.30

$Fe_2O_3^t$ – total iron; LOI – loss on ignition; A/CNK – molar $Al_2O_3/CaO + Na_2O + K_2O$; ∑REE – sum of the total REE; Eu* – $\sqrt{(Sm_N) \times (Gd_N)}$; BDL – below detection limit; REE normalization based on Taylor & McLennan (1985).

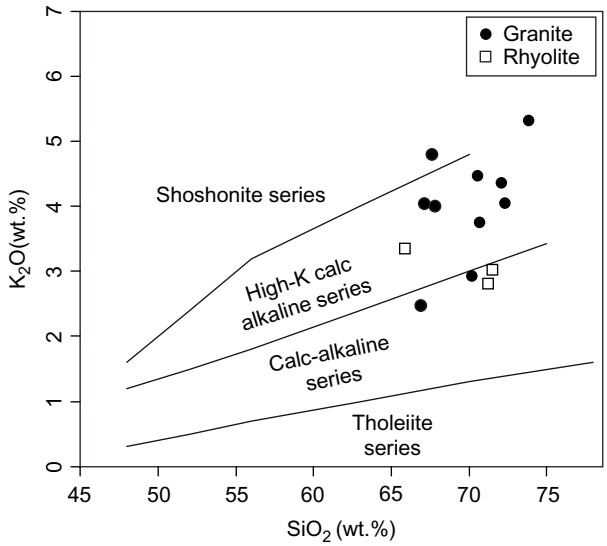

Fig. 5. K_2O versus SiO_2 plot for the studied granites and rhyolites (fields are shown after Peccerillo & Taylor, 1976).

(Fig. 7). The contents of TiO_2, MgO, CaO, FeO^t and Al_2O_3 show a decreasing trend with increasing SiO_2 for both the granites and rhyolites (Fig. 8). On the Nb versus Y tectonic discrimination diagram (Pearce *et al.* 1984), all the studied samples plot in the volcanic arc granite (VAG) plus syn-collisional granite (syn-COLG) fields (Fig. 9a), and on the Rb versus Y + Nb diagram they plot in the VAG field (Fig. 9b). The granites SM 8 and SM 9 most likely originated from metapelite, as evident from the observed low to moderate Mg no. (11.7–57.6), and high Na_2O (3.63–4.62), Tb_N/Yb_N (3.0–9.1), $Al_2O_3/(MgO + FeO^t)$ (7.0–35.5) and K_2O/Na_2O (0.5–1.4), as typically suggested elsewhere for melts generated from metapelites (Altherr *et al.* 2000).

The total sum of REEs for the granites varies from 50.43 to 299.47 ppm and for the rhyolites from 115.9 to 167.7 ppm. The rhyolites exhibit almost similar chondrite-normalized (Taylor & McLennan, 1985) REE patterns to those observed for the granites, with moderate negative europium anomalies (Eu_N/Eu^* =0.75–0.84) compared to the granites, which show a wide range of negative to positive europium anomalies (Eu_N/Eu^* = 0.25–1.13) (Fig. 10a; Table 1). The light rare earth element (LREE) patterns are inclined, whereas the heavy rare earth elements (HREEs) exhibit almost flat patterns, suggesting moderate LREE to HREE fractionation (La_N/Lu_N = 11.29 to 177.1) for the studied granites and rhyolites. However, the LREE to HREE fractionation (La_N/Lu_N = 11.29 to 177.1) of the granites is slightly more than that observed for the rhyolites (La_N/Lu_N = 15.68–16.60).

The primitive mantle-normalized (Taylor & McLennan, 1985) trace-element patterns of the granites and rhyolites show enriched large ion lithophile element (LILE) patterns relative to the high field strength elements (HFSE). The observed negative Nb, Sr, Ti and V anomalies for the granites suggest subduction-related calc-alkaline magmatism (Kelemen *et al.* 1993). The rhyolites also show negative Nb–Sr anomalies, but a slight enrichment in Ti, V and Ni contents compared to those observed for the granites (Fig. 10b).

5. Zircon U–Pb geochronology

We selected five granite samples (SM 8, SM 9, SM 16, SM 17, SM 20) and one rhyolite sample (SM 22) from the KB for zircon U–Pb geochronology to constrain the timing of magmatic events. Online Supplementary Material Table S2 presents the LA-MC-ICP-MS analysed zircon U–Pb geochronological database for the granites and rhyolite. The details are as follows.

5.a. SM 8 (granite)

The zircons from SM 8 are euhedral, showing oscillatory zoning patterns with bright cores (Fig. 11a). We analysed 25 zircon spots on 17 zircon grains. The Th/U ratio of 13 zircon cores and rims varies from 0.02 to 0.07, while ten analyses show a relatively high Th/U ratio of 0.17–0.57, and two zircon cores show a very high Th/U ratio of 27.2 and 30.5 (online Supplementary Material Table S2). Although low Th/U (<0.2) and high Th/U (>0.2) ratios have been suggested for zircons of metamorphic and magmatic origins, respectively (Rubatto & Gebauer, 2000; Hoskin & Schaltegger, 2003), no clear distinction regarding the mode of origin of zircons can be made on the basis of Th/U ratio alone. However, the sharp contacts between the oscillatory zoned rims and cores with a high Th/U ratio (>0.2) observed for most of the zircon grains indicates a magmatic origin. The data for all the zircon spot analyses were plotted on a concordia diagram, on which the analyses from the rims suggest an age range of middle to late Miocene (18.2–10.22 Ma), while the ages from the cores vary from Palaeoproterozoic to Late Cretaceous (2028–80 Ma), suggesting their inheritance from the Karakoram basement (Fig. 12a). The seven most concordant analyses from the zircon rims yield a ^{206}Pb–^{238}U weighted mean age of 15.029 ± 0.01 Ma (MSWD = 1.34), which can be interpreted as the crystallization age of the zircons in the granite (Fig. 12b). Inherited zircon grains yield ages of 80, 787, 1170, 1830 and 2028 Ma, which indicate the involvement of heterogeneous sources in the genesis of the granite.

5.b. SM 9 (granite)

The zircons from SM 9 are mostly euhedral and oscillatory zoned with weakly zoned rims having some homogeneous

https://doi.org/10.1017/S0016756819001547 Published online by Cambridge University Press

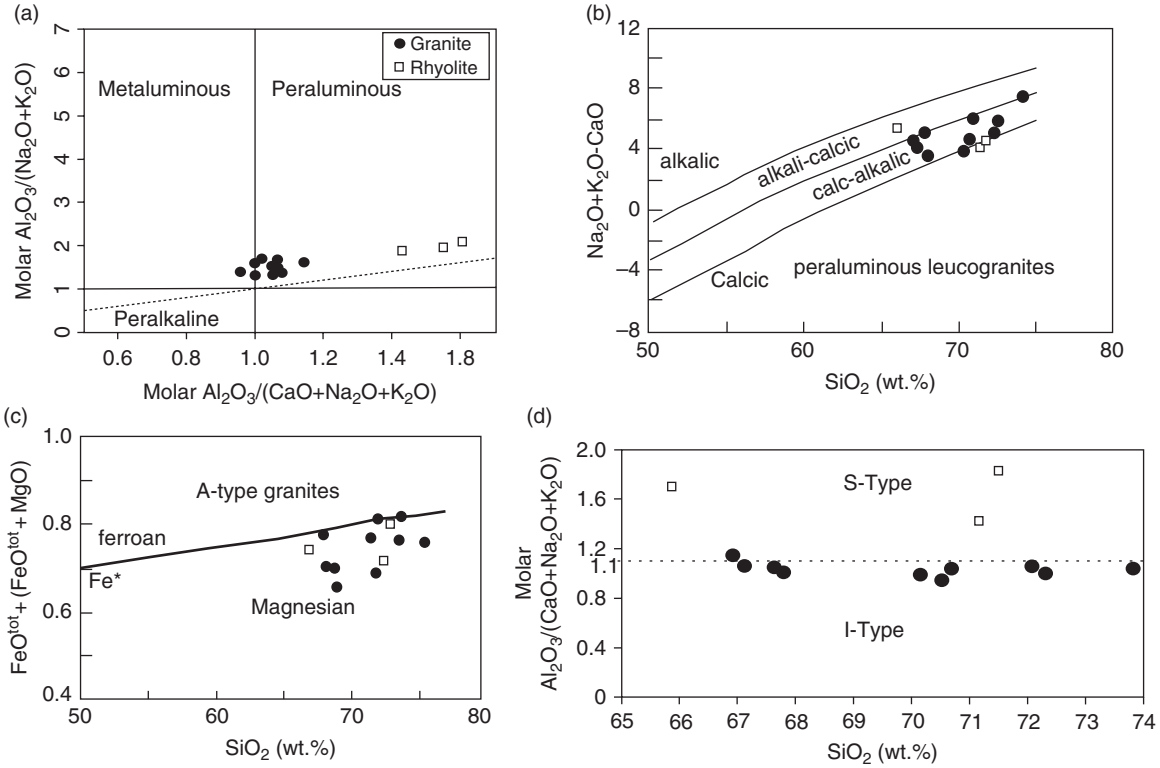

Fig. 6. Major element-based geochemical classification plots for granites and rhyolites. (a) Molar A/NK ($Al_2O_3/Na_2O + K_2O$) versus molar A/CNK ($Al_2O_3/CaO + Na_2O + K_2O$) plot (discrimination fields after Maniar & Piccoli, 1989). (b) Plot of $Na_2O + K_2O$–CaO against SiO_2 showing the approximate ranges for the alkalic, alkali–calcic, calc-alkalic and calcic rock series (after Frost *et al.* 2001). (c) FeO/(FeO^t + MgO) versus wt % SiO2 diagram showing the boundary between ferroan plutons and magnesian plutons (after Frost *et al.* 2001). (d) Molar A/CNK ($Al_2O_3/CaO + Na_2O + K_2O$) versus SiO_2 plot (fields after Chappell & White, 1974).

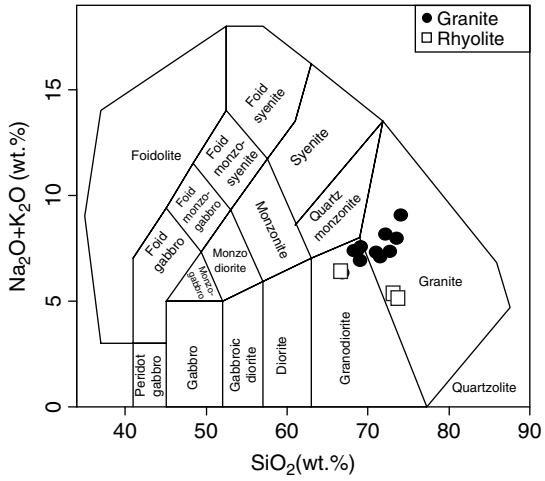

Fig. 7. Total alkali silica (TAS) plot (fields after Cox *et al.* 1979).

domains. The cores are bright with sharp to transgressive contacts, but the rims show features of recrystallization (Fig. 11b). Thirty-one analyses on 19 zircon grains were carried out. The data for all analyses were plotted on a concordia diagram, on which all 12 analyses from the rims suggest an age of middle to late Miocene (14.96–11.62 Ma), except two analyses with Late Cretaceous and early Palaeogene ages (67 Ma and 57 Ma), while the other ten analyses from the cores vary from Mesoproterozoic to Late Cretaceous (1969–65 Ma) in age, suggesting inheritance from the Karakoram basement (Fig. 12c). The five most concordant analyses from the zircon rims yield a ^{206}Pb–^{238}U weighted mean age of 12.680 ± 0.26 Ma (MSWD = 2.62), which is interpreted as the zircon crystallization age in the granite (Fig. 12d). Inherited zircon ages from the cores cluster in the groups 57–70 Ma, 95.6–205 Ma, 418.8–696 Ma, 1382 Ma and 1969 Ma, which strongly points to the recycling of heterogeneous older sources in the genesis of the granite.

5.c. SM 16 (granite)

The zircons from sample SM 16 are subhedral to euhedral, showing oscillatory zoning developed over the bright cores (Fig. 11c). Thirty spots on 18 zircon grains were analysed. Twenty-three zircon analyses have high measured Th/U ratios (0.20–1.99), which indicate a magmatic origin (Rubatto & Gebauer, 2000). Seven analyses from the zircon rims and cores have measured Th/U ratios of between 0.05 and 0.18, indicating a metamorphic or recrystallized origin for the zircon grains (online Supplementary Material Table S2). Data for all of the 30 analyses were plotted on a concordia diagram, on which 26 analyses suggest Early to Late Cretaceous ages (86.3–45.4 Ma), while three analyses from the inherited cores show Palaeozoic ages (379 Ma, 349 Ma and 579 Ma), with a single rim analysis showing an Eocene age (52.6 Ma) (Fig. 12e). The seven most concordant zircon analyses yield a ^{206}Pb–^{238}U weighted mean age of 99.38 ± 0.89 Ma (MSWD = 0.75), whereas six zircon analyses yield a ^{206}Pb–^{238}U weighted mean age of 105.62 ± 1.75 (MSWD = 2.94). These ages at least indicate two episodes of granite magmatism in Middle Cretaceous time (Fig. 12f). Inherited zircon core ages vary from 349 to 519 Ma, which probably indicates the involvement of juvenile and Gondwana components in the origin of the granite.

https://doi.org/10.1017/S0016756819001547 Published online by Cambridge University Press

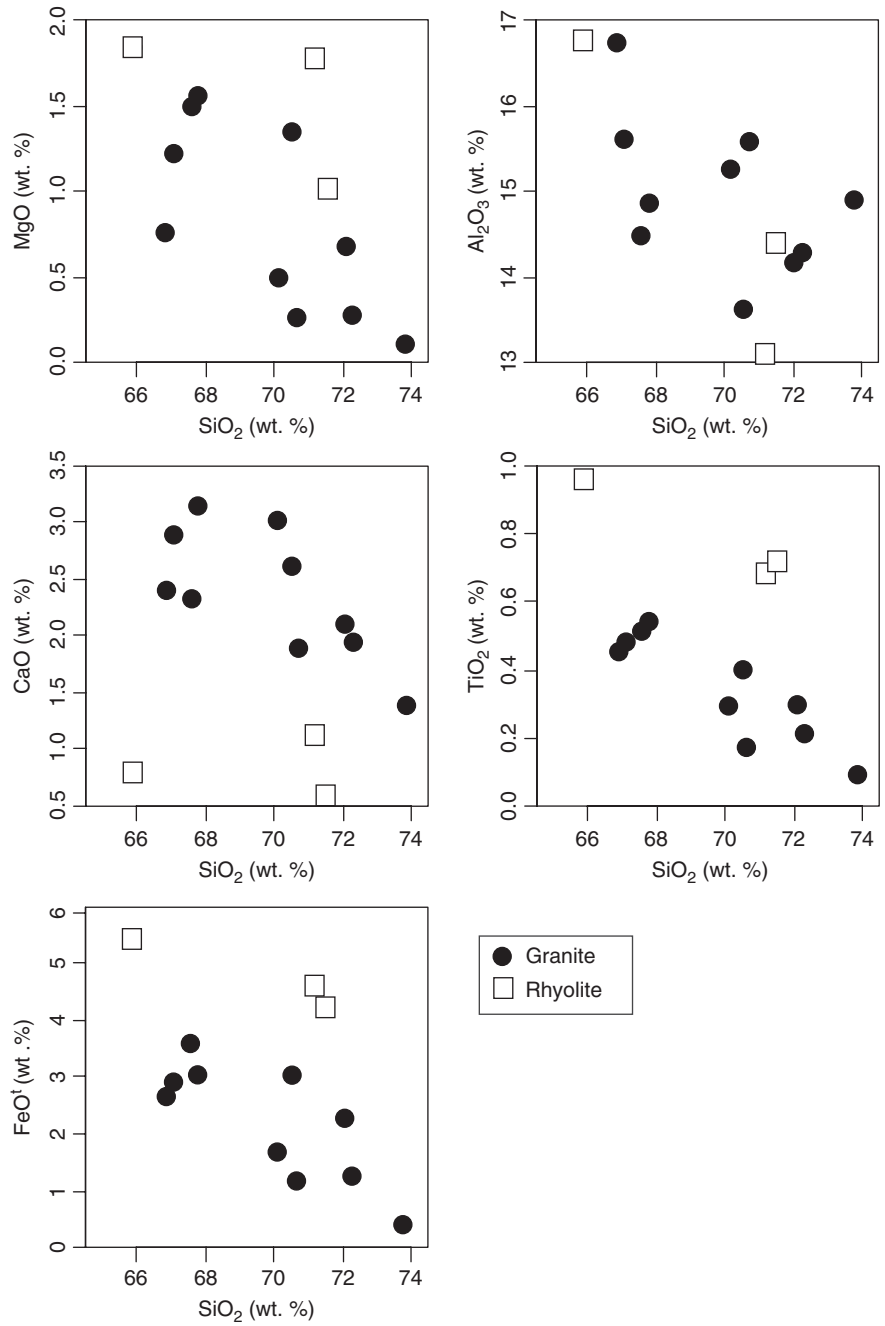

Fig. 8. Harker variation plots as major oxides (wt %) versus SiO_2 (wt %) for the granites and rhyolites.

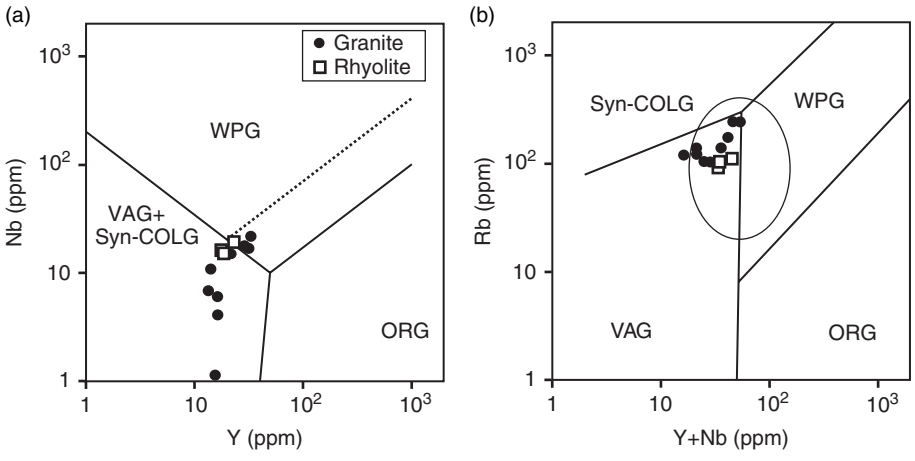

Fig. 9. Tectonic discrimination diagrams to identify the tectonic setting of the analysed samples. (a) Nb versus Y tectonic discrimination diagram (Pearce *et al.* 1984), and (b) Rb versus Y + Nb tectonic discrimination diagram (Pearce *et al.* 1984). VAG – volcanic arc granite; syn-COLG – syn-collisional granite; WPG – within-plate granite; ORG – ocean ridge granite.

https://doi.org/10.1017/S0016756819001547 Published online by Cambridge University Press

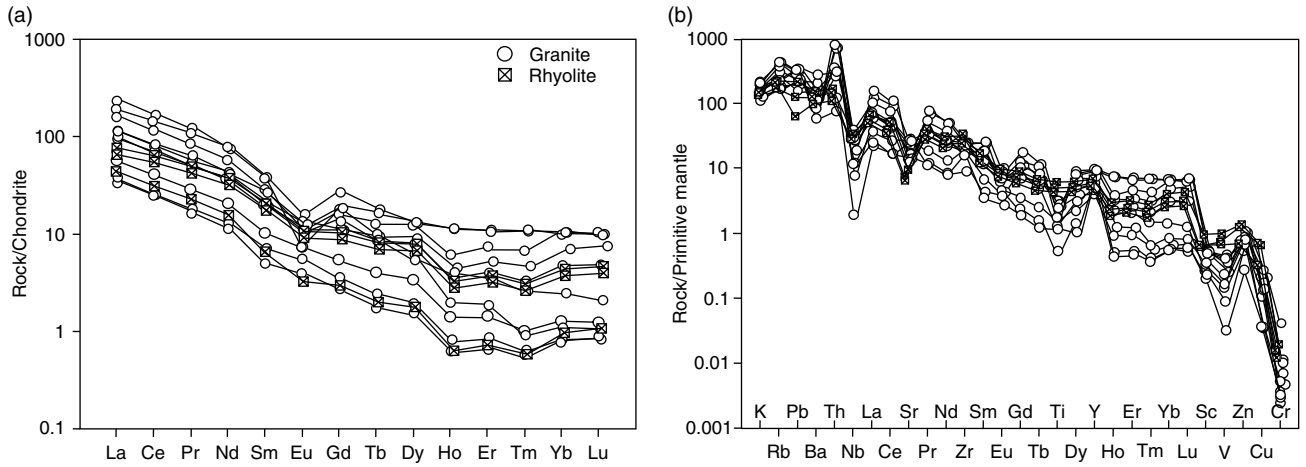

Fig. 10. (a) Chondrite-normalized (Taylor & McLennan, 1985) rare earth element diagram plotted for the analysed samples. (b) Primitive mantle-normalized (Taylor & McLennan, 1985) trace-element spider diagram plotted for the analysed samples.

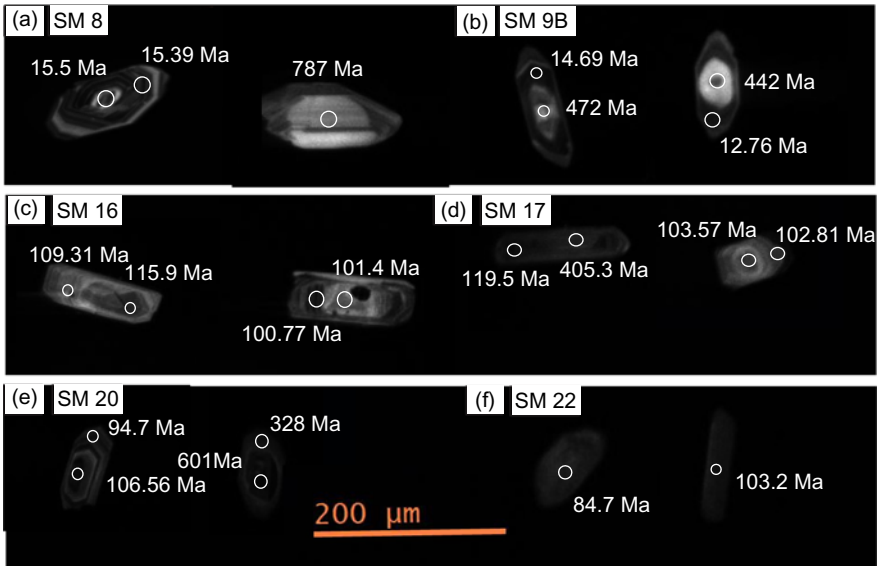

Fig. 11. (Colour online) Cathodoluminescence images of representative zircons from the analysed samples. (a) SM 8; (b) SM 9A; (c) SM 16; (d) SM 17; (e) SM 20; (f) SM 22.

5.d. SM 17 (granite)

The zircons from SM 17 are mostly subhedral, having oscillatory zoned to weakly zoned rims (Fig. 11d). Thirty analyses on 20 grains were carried out. The Th/U ratio for all the analyses is >0.2 (0.22–0.90), indicating a magmatic origin for the zircons, except a single analysis from a rim (Th/U = 0.13). All the 30 analyses were plotted on a concordia diagram, on which 27 analyses suggest an age of Early to Late Cretaceous (130–86.2 Ma), while three inherited zircon cores show Palaeozoic to Neoproterozoic ages (405, 536 and 741 Ma) (Fig. 13a). The six most concordant analyses yield a ^{206}Pb–^{238}U weighted mean age of 104.52 ± 0.75 Ma (MSWD = 2.03), interpreted as the zircon crystallization age in the granite (Fig. 13b). Inherited ages from the zircon cores vary from 405.3 to 741 Ma, which suggests their source is Gondwanaland.

5.e. SM 20 (granite)

The zircons from SM 20 are euhedral and oscillatory zoned. Inherited zircon cores can be seen with sharp to somewhat diffusive contacts (Fig. 11e). Thirty analyses on 18 zircon grains were carried out. Th/U ratios for most of the analyses are higher than 0.2 (0.20–1.0), indicating a magmatic origin, while some zircon cores and rims have measured Th/U ratios of between 0.09 and 0.19 (online Supplementary Material Table S2). All the 30 analyses were plotted on a concordia diagram, on which 18 analyses suggest an age of Early to Late Cretaceous (142–92.1 Ma), while the nine inherited zircon cores suggest Palaeoproterozoic to Palaeozoic ages (1601–328 Ma) (Fig. 13c). The five most concordant zircon analyses yield a ^{206}Pb–^{238}U weighted mean age of 108.03 ± 0.61 Ma (MSWD = 2.52), interpreted as the zircon crystallization age in the granite (Fig. 13d). Inherited zircon ages from this sample vary in the age groups 328–702 Ma and 1193–1601 Ma, which suggests the involvement of Meso- to Neoproterozoic and some younger crustal components in the genesis of this granite.

5.f. SM 22 (rhyolite)

The zircon grains from SM 22 are mostly homogeneous with some faint oscillatory zoning patterns (Fig. 11f). Thirty analyses on 24 zircon grains were carried out, mostly on the cores because the rims were too thin to perform the analysis. Th/U ratios for most of the

https://doi.org/10.1017/S0016756819001547 Published online by Cambridge University Press

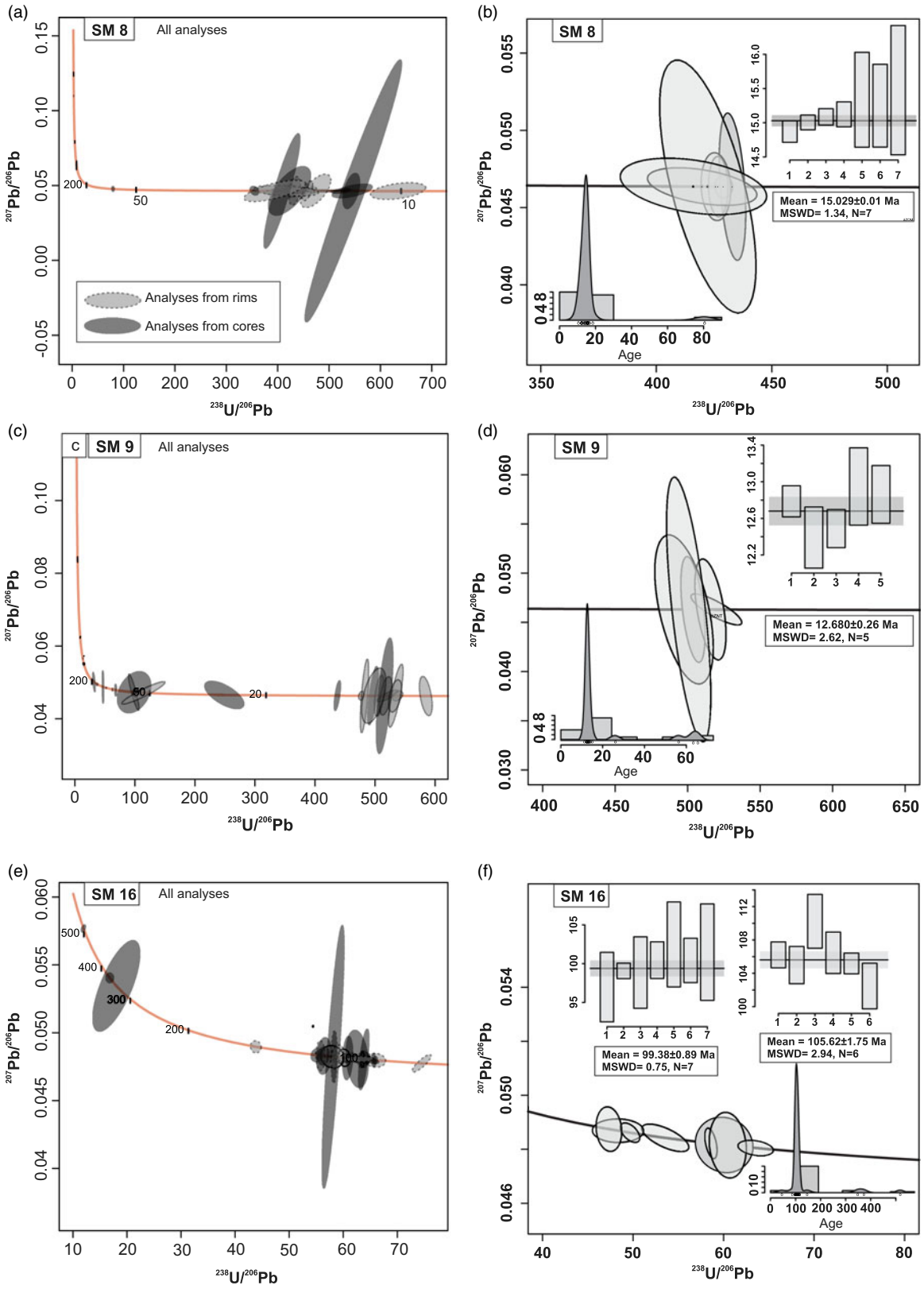

Fig. 12. (Colour online) ^{206}Pb–^{238}U ages and concordia diagrams for LA-MC-ICP-MS zircon data plots. (a) SM 8, all data analyses; (b) SM 8, most concordant ages showing crystallization age. (c) SM 9A, all data analyses; (d) SM 9A, most concordant ages showing crystallization age. (e) SM 16, all data analyses; (f) SM 16, most concordant ages showing crystallization age.

https://doi.org/10.1017/S0016756819001547 Published online by Cambridge University Press

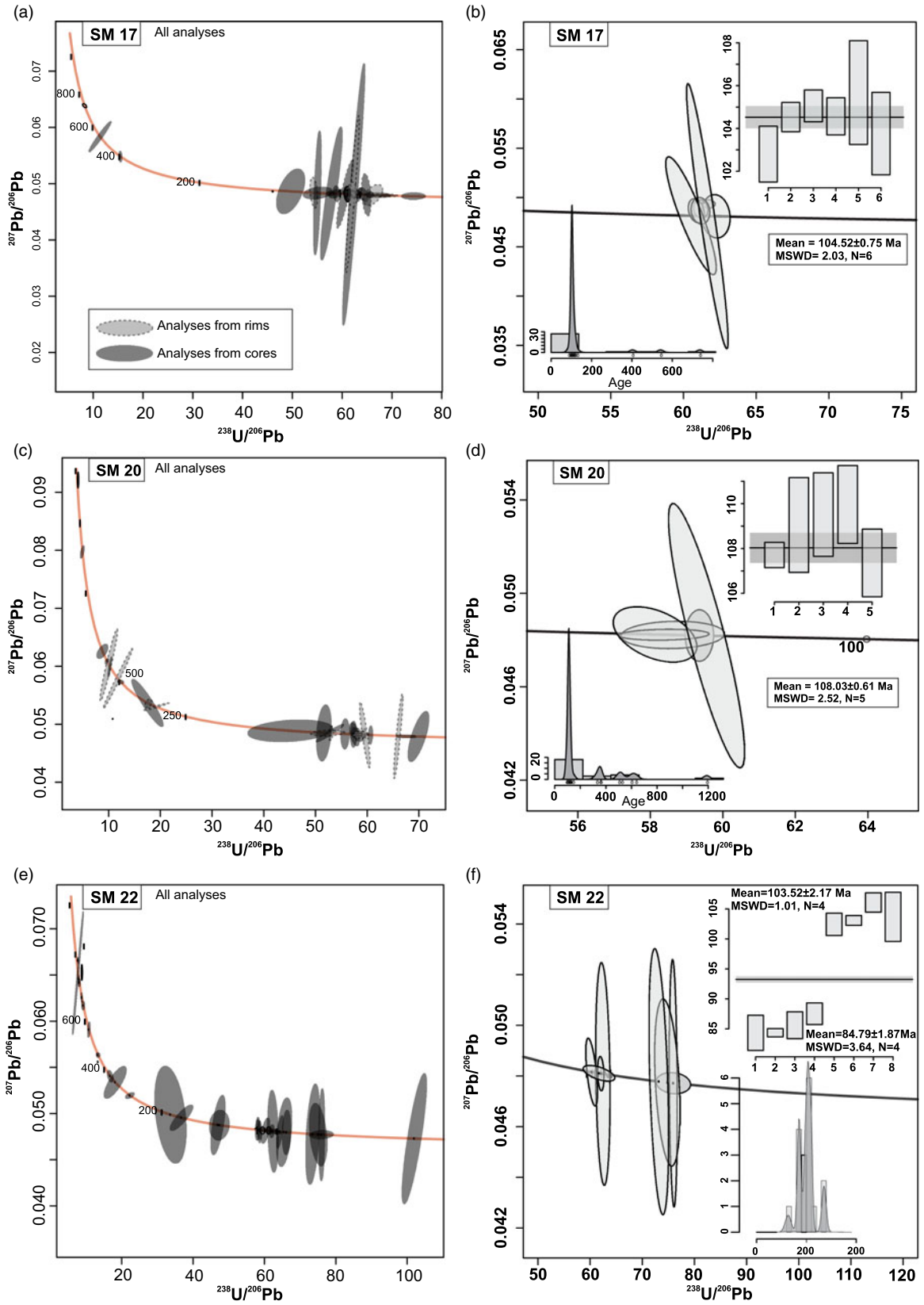

Fig. 13. (Colour online) ^{206}Pb–^{238}U ages and concordia diagrams for LA-MC-ICP-MS zircon data plots. (a) SM 17, all data analyses; (b) SM 17, most concordant ages showing crystallization age. (c) SM 20, all data analyses; (d) SM 20, most concordant ages showing crystallization age. (e) SM 22, all data analyses; (f) SM 22, most concordant ages showing crystallization age.

https://doi.org/10.1017/S0016756819001547 Published online by Cambridge University Press

zircon analyses are >0.2 (0.20–2.1), indicating a magmatic origin, while some analyses have Th/U ratios of between 0.11 and 0.19 (online Supplementary Material Table S2). All the 30 analyses were plotted on a concordia diagram, on which 17 analyses suggest an age of Early to Late Cretaceous (~136.6–65.8 Ma), three analyses an age of Early to Middle Jurassic (192–175 Ma) and 11 analyses a Permian age (782–284 Ma) (Fig. 13e). The ages from the rhyolite can be divided into three groups: Coniacian to Santonian within the Late Cretaceous (89.7–84.7 Ma with Th/U = 0.73–2.1), Early to Late Cretaceous (136.6–98.4 Ma with Th/U = 0.405–0.893) and Neoproterozoic to Middle Jurassic (782–175 Ma with Th/U = 0.11–1.3).

The four most concordant zircon analyses yield a ^{206}Pb–^{238}U weighted mean age of 103.52 ± 2.17 (MSWD = 1.01), while a cluster of another four zircon analyses (Th/U = 0.73–2.1) yield a ^{206}Pb–^{238}U weighted mean age of 84.79 ± 1.87 (MSWD = 3.64) (Fig. 13f). These two age peaks corresponding to the Late Cretaceous are observed on the Kernel density estimate (KDE) plot (Fig. 13f). Inherited zircon ages from this sample vary in the age groups 175–284 Ma and 343–782 Ma, which indicates the contribution of Permian to Middle Jurassic and Neoproterozoic to Late Palaeozoic components in the evolution of the rhyolite.

6. Discussion

6.a. Process diagnosis and likely tectonic settings of the granites and Murgo Volcanics

The studied granites and rhyolites from the Shyok Valley region are undeformed and do not show evidence of mylonitization and migmatization, as commonly observed near the KFZ. The granites are metaluminous to weakly peraluminous (S-type; molar A/CNK = 0.95–1.14), which might be due to evolution through fractional crystallization of calc-alkaline, metaluminous (I-type) parental magma giving rise to a mildly peraluminous residual melt. However, the rhyolites are strongly peraluminous (S-type) in nature (molar A/CNK = 1.42–1.81), which could have been formed by AFC. TiO_2, MgO, CaO, FeO^t and Al_2O_3 behave as compatible elements in both granites and rhyolites, which equivocally dictates that their evolution is dominantly controlled by fractionation of biotite, plagioclase, K-feldspar and sphene (Fig. 8) from calc-alkaline, magnesian-type felsic parental melts (Fig. 6).

Slab dehydration during subduction leads to the release of fluids that carry mobile elements into the overlying mantle wedge, which is a common feature of arc environments (Keppler, 1996; Xiao *et al.* 2016). These fluids from the subduction zone interact with the fluids of the mantle wedge, and form hydrous minerals (e.g. hornblende, biotite), which are present in the studied granites (Fig. 4) (e.g. Murphy, 2006). Enrichment of the LILEs in the granites suggests that the mobile elements (e.g. K, Rb, Ba, Sr, U, Th) extracted from the subducted slab through supercritical fluid have enriched the overlying mantle wedge, and this is recorded in the contents of trace elements in the samples (Fig. 10b; Table 1) (e.g. Spandler *et al.* 2003; Murphy, 2006). The enrichment of LREEs relative to HREEs with moderately negative to mildly positive Eu anomalies (Eu_N/Eu^* = 0.25–1.13) in the granites (Fig. 10a; Table 1) would have been controlled mainly by plagioclase fractionation and little plagioclase accumulation, respectively, during the evolution of the parental granite magma. The presence of negative Eu anomalies (Eu_N/Eu^* = 0.75–0.84) in the rhyolites suggests plagioclase fractionation during their evolution. The total sum of REEs for the granites (172.2 ppm; n = 10; SiO_2 = 66.92–73.85 wt %) and rhyolites (137.6 ppm; n = 3; SiO_2 = 65.88–71.49 wt %) and the average LREE/HREE fractionation (La_N/Lu_N = 44.10 for the granites and La_N/Lu_N = 16.28 for the rhyolites) points to the relatively more evolved nature of the granites compared to the rhyolites (Table 1). Both the granites and rhyolites exhibit LILE enrichment (e.g. Th, K, Ba) and HFSE depletion (e.g. Nb, Ti, Zr) with negative Nb, Ti and Zr and positive Th anomalies with respect to primitive mantle values (Fig. 10b), which are mostly sourced from the subducting lithosphere, which induced melting of the mantle wedge. Tectonic discrimination via major oxides (Maniar & Piccoli, 1989) also shows that the granites and rhyolites belong to continental arc granitoids (CAG) of the orogenic field. The granites (SM 10–SM 20) and the rhyolites bear high Mg nos. (100Mg/Mg + Fe) ranging from 27.3 to 69.4 and from 51.4 to 62.6, respectively. We observed low Na_2O contents for the granites (2.84–4.26 wt %) and rhyolites (2.19–2.90 wt %) and high abundances of incompatible elements, and $(Tb/Yb)_N$ = 1.29–3.3 and 1.73–1.87, respectively, for the granites and rhyolites. These characteristics suggest an origin from enriched lithospheric mantle sources (Altherr *et al.* 2000). The rhyolites are calc-alkaline with low HFSEs and high Zr/Y (10.4–15.6) and La_N/Yb_N (16.7–17.3), which corresponds to the FI group of rhyolites typically formed in subduction settings (Lesher *et al.* 1986).

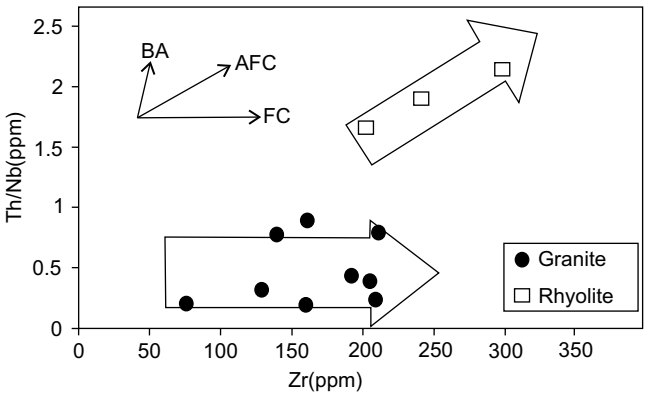

Fig. 14. Th/Nb versus Zr plot for the studied samples. Trends reflect increasing fractional crystallization (FC), assimilation fractional crystallization (AFC) and bulk assimilation (BA) (after Nicolae & Saccani, 2003).

In the eastern Karakoram, the exposed felsic magmatic rocks in the Nubra–Shyok Valley are represented by calc-alkaline metaluminous (I-type) Tirit granites (Rao & Rai, 2009; Kumar *et al.* 2017), while the Panamik granites exposed in the Khalsar–Panamik (Fig. 1c) area are weakly peraluminous (Rao & Rai, 2009), similar to those noted for the studied granites from the Shyok–Murgo section (Fig. 1c). In contrast, the rhyolites exhibit elevated molar A/CNK (with enriched LILEs and LREEs), which may suggest derivation from pelitic sources present in the accretionary wedge or the crustal basement (e.g. Thorpe, 1982). The observed moderate to high K_2O (2.48–5.33 wt %) and $K_2O > Na_2O$ with enrichment of Rb content (95–240 ppm) for the granites; and K_2O (2.83–3.37 wt %) and $K_2O > Na_2O$ with high Rb content (94–118 ppm) for the rhyolites also advocates for varying amounts of crustal contribution in their genesis. The Th/Nb versus Zr plot (Fig. 14) for the granites shows a continuously increasing Zr trend with slight enrichment in Th/Nb that suggests fractional crystallization as the dominant process in the evolution of the granites (e.g. Nicolae & Saccani, 2003). On the other hand, the rhyolites demonstrate an increasing trend of Th/Nb with Zr that suggests the dominant role of AFC during magmatic differentiation (Fig. 14).

https://doi.org/10.1017/S0016756819001547 Published online by Cambridge University Press

On the Rb versus Y + Nb plot (Fig. 9b), the granites and rhyolites lie within an ellipse approaching a triple point formed by the intersection of the boundary lines separating the VAG, syn-COLG and within-plate granite (WPG) fields, which is the region of post-collisional granites (Pearce, 1996). The observed enrichment of Rb and K_2O, and high A/CNK ratios in the granites and rhyolites can be most likely achieved through AFC. However, the major oxide contents demonstrate the continental arc nature of the rhyolites (Fig. 6b).

6.b. Quantitative modelling of fractional crystallization and assimilation

During fractional crystallization, the magma simultaneously assimilates the surrounding rocks of the crust because of heat transfer from the hot magma to the more cold surroundings (Kuritani *et al.* 2005). The deep lower crustal rocks in the Karakoram terrane are mainly igneous and high-grade metamorphic rocks (Searle, 2015). In the study area, the main bedrock is highly evolved Late Cretaceous granites that contain older crustal components such as Palaeozoic and Proterozoic zircons, as recorded in the present work and elsewhere (Kumar *et al.* 2017 and references therein). Geochemically, these granites are slightly peraluminous to metaluminous, and enriched in the LILEs (e.g. Sr, Rb, Ba). The rhyolites are strongly peraluminous and exhibit xenocrystic magmatic zircons derived from the KB pluton, which can be explained based on the trace-element (U, Th) composition of the zircons. The zircons from the rhyolite sample SM 22 have Late Cretaceous ages (84.7 to 89.7 Ma) with high Th/U ratios (0.73–2.1), while the other xenocrystic zircons of Early to Late Cretaceous and Neoproterozoic to Middle Jurassic ages have Th/U ratios of between 0.40–0.9 and 0.11–1.3, which correlates well with the observed Th/U ratios (0.06–1.1) of the zircons from the granites (SM 16–SM 20). Hence, we prefer these granites as the potential candidates for contaminants during synchronous fractional crystallization. We suggest that the rhyolite magma was formed by fractional crystallization of a more primitive magma at depth accompanied by assimilation of the KB.

An attempt was made to quantitatively constrain the likely processes of assimilation of the pre-existing granites by the rhyolites accompanied by fractional crystallization using trace elements, including the REEs of the rhyolite and assimilant granite, and the Microsoft Excel-based Petromodeler program containing partitioning coefficients (Kds) of the Geochemical Earth Reference Model (GERM) database (Ersoy, 2013). To quantitatively model the fractional crystallization forming the cogenetic granites, we assumed the least fractionated sample SM 13 as the starting parental magma composition (Co^f). An increasing degree of F, i.e. the fraction of remaining melt, was used to test the fractionation of this parental magma. The REE content of the highly evolved SM 10 granite as a residual melt with $SiO_2 = 72.29$ wt % can be achieved at F = 37 %, which at least constrains the evolved nature of the granite melt through 63 % fractional differentiation (Fig. 15).

For modelling the AFC, we considered the rhyolite sample SM 23 to be the least contaminated or uncontaminated sample, because of its extremely low content of incompatible elements (e.g. Sr, U, La,), and granite sample SM 14 of the KB as the assimilant (Fig. 16a, b). The average of the pre-collision granites (SM 10 and SM 20) was also used as a possible contaminant (Fig. 16c, d). The obtained results dictate that rhyolite SM 21 can be achieved by assimilation of ~34.5 % (r = 0.13; the ratio of assimilation rate and fractional crystallization rate) of granite SM 14 by rhyolite SM 23

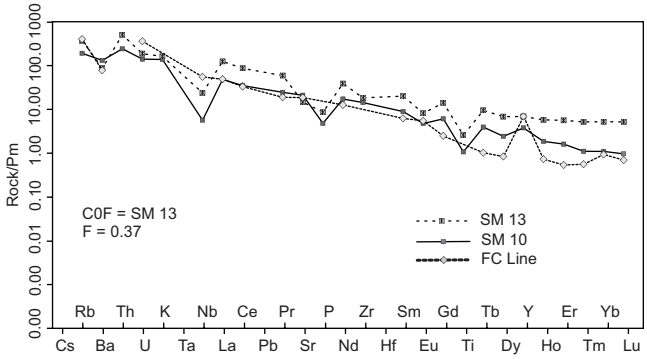

Fig. 15. Plots demonstrating the quantitative models of fractional crystallization (FC) using the Petromodeler program (after Ersoy, 2013).

(Fig. 16a). Rhyolite SM 22 can be produced by ~13.8 % (r = 0.40) assimilation of rhyolite SM 23 with granite SM 14 (Fig. 16b). The rhyolites SM 21 and SM 22 can also be achieved by ~34.5 % (r = 0.10) and ~13.8 % (r = 0.15) assimilation of the average pre-collisional granites as contaminants (Fig. 16c, d). The likely higher degree of assimilation might have occurred owing to a second boiling prevailing in the chamber (Sisson & Bacon, 1999). Further, the latent heat of crystallization of the anhydrous groundmass minerals may induce the effect of a second boiling (Kumar, 2014). The obtained quantitative models at least constrain the evolution of the rhyolites through AFC. The future work on whole-rock Sr–Nd isotopes of the granites and rhyolites can strengthen our proposed model of AFC.

6.c. Episodic magmatism in the evolution of the Karakoram Batholith

Several earlier attempts have been made to understand the contribution of magmatism in the evolution of the KB. Weinberg *et al.* (2000) reported the U–Pb zircon crystallization age of ~68 Ma as the emplacement age for the Tirit granites exposed along the Nubra–Shyok Valley and correlated this part with an equivalent magmatic episode of the Ladakh Batholith. Upadhyay (2008) reported a more or less similar emplacement age of ~71 Ma for the Tirit granites. However, Kumar *et al.* (2017) reported ~109–105 Ma ages for the calc-alkaline Tirit granites and opined that subduction along the SSZ started much earlier in Early Cretaceous time. Our results are similar to the observations of Ravikant *et al.* (2009), who reported ~103–100 Ma ages for zircon crystallization in enclaves from the Skyangpoche region and concluded that the subduction along the SSZ might have initiated at ~103 Ma, i.e. much earlier than along the ITSZ. However, studies from the western Karakoram by Heuberger *et al.* (2007) suggested that the subduction started still earlier again at ~121 Ma, as evident from the U–Pb zircon crystallization age of the Tirich Mir pluton. In the present study, zircon dating from three granite samples (SM 16, SM 17 and SM 20) points to episodic magmatism spanning ~108 to 100 Ma (Figs 12e, f, 13a–d).

Zircon U–Pb geochronological data from previous and present studies on the volcano-plutonic magmatic rocks of the KLA and Karakoram Block have been compiled and processed in order to plot an age probability diagram (Fig. 17). Two main pre-collisional magmatic episodes in the Karakoram Block during Early Cretaceous time (125–99 Ma) and Late Cretaceous to Palaeogene times (85–50 Ma) can be recognized (Fig. 17a). However, there is a significant magmatic gap observed between

https://doi.org/10.1017/S0016756819001547 Published online by Cambridge University Press

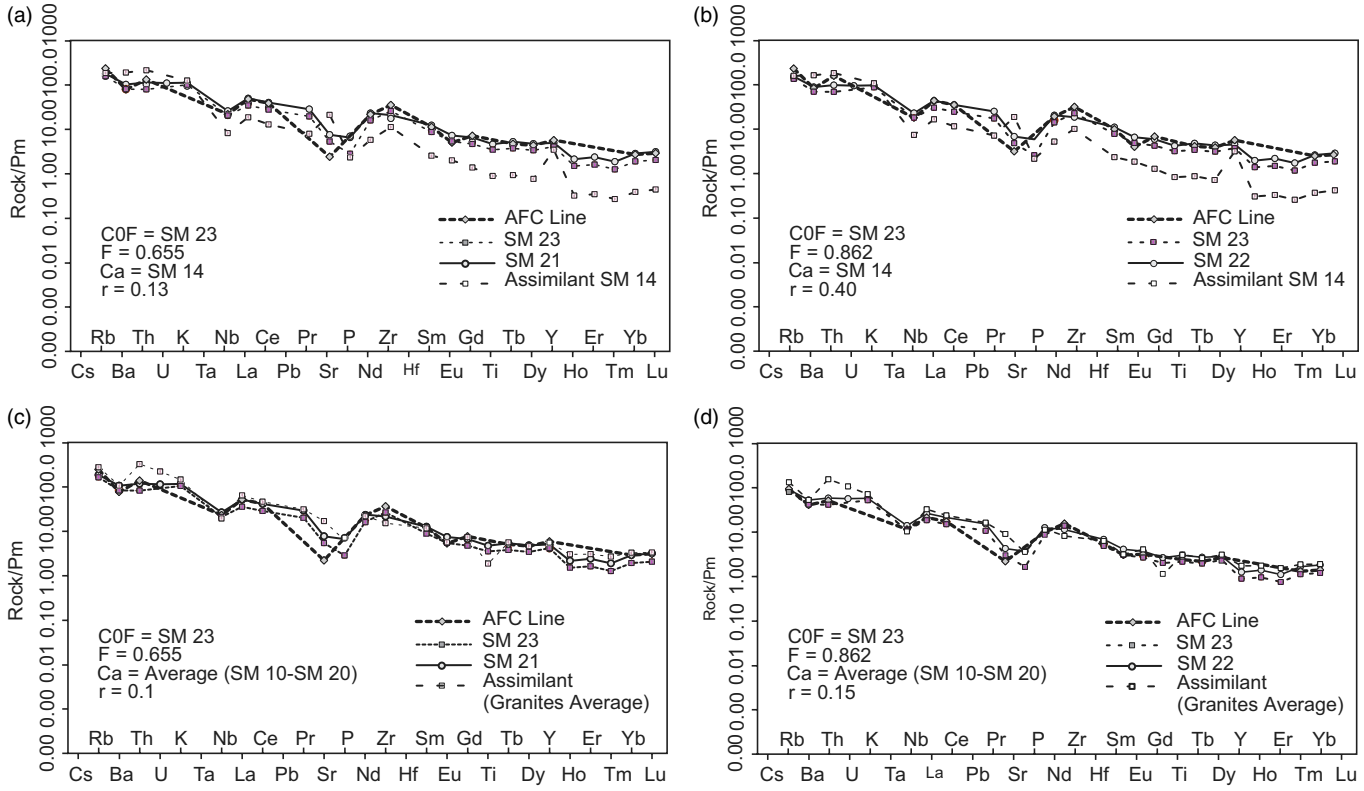

Fig. 16. Plots demonstrating the quantitative models of assimilation accompanied by fractional crystallization (AFC). (a) Assimilation of rhyolite SM 23 and granite SM 14 producing rhyolite sample SM 21; (b) assimilation of rhyolite SM 23 and granite SM 14 producing rhyolite sample SM 22; (c) assimilation of rhyolite SM 23 and the average of KB granites producing rhyolite sample SM 21; (d) assimilation of rhyolite SM 23 and the average of KB granites producing rhyolite sample SM 22 using the Petromodeler program (after Ersoy, 2013).

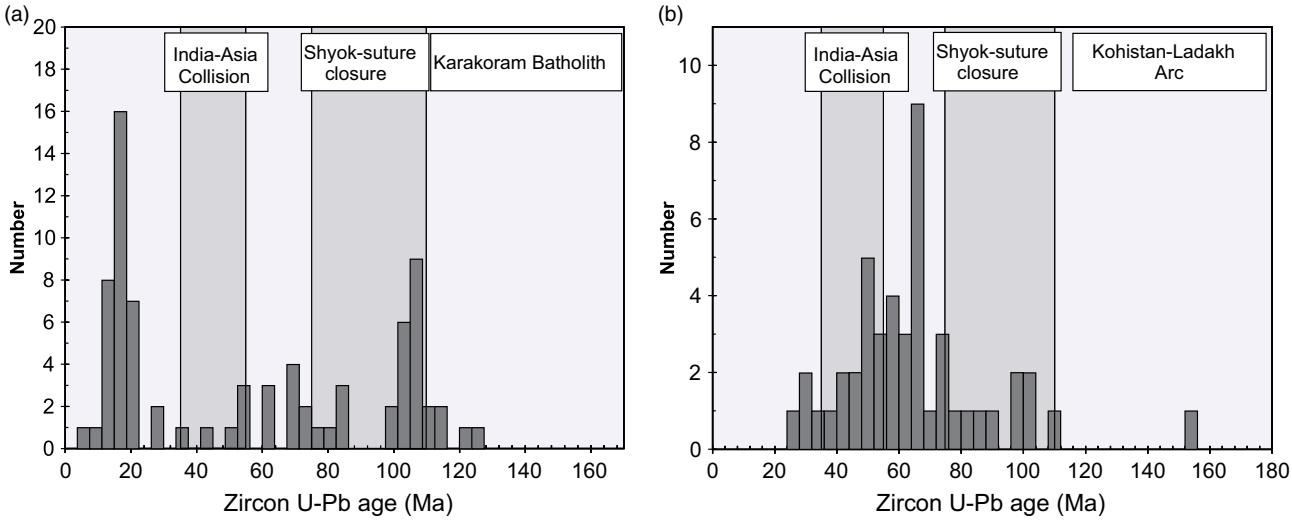

Fig. 17. Zircon ^{206}Pb–^{238}U age probability diagram for rocks from (a) the Karakoram Batholith; and (b) the Kohistan-Ladakh Arc. Data from present study and: a – Desio *et al.* (1964); b – Honegger *et al.* (1982); c – Parrish & Tirrul (1989); d – Schärer *et al.* (1984); e – Khan *et al.* (1996); f – Krol *et al.* (1996); g – Searle *et al.* (1998); h – Weinberg & Dunlap (2000); i – Weinberg *et al.* (2000); j – Fraser *et al.* (2001); k – Hildebrand *et al.* (2000); l – Dunlap & Wysoczanski (2002); m – Schaltegger *et al.* (2002); n – Phillips *et al.* (2004); o – Heuberger *et al.* (2007); p – Singh *et al.* (2007); q – Jain & Singh (2008); r – Upadhyay (2008); s – Jagoutz *et al.* (2009); t – Ravikant *et al.* (2009); u – Boutonnet *et al.* (2012); v – Phillips *et al.* (2013); w – Borneman *et al.* (2015); x – van Buer *et al.* (2015); y – Kumar *et al.* (2017); z – Sen *et al.* (2018). India–Asia collision data from: a – Searle *et al.* (1987); b – Klootwijk *et al.* (1992); c – Rowley (1996); d – Najman *et al.* (2010); e – Bouilhol *et al.* (2013); f – Hu *et al.* (2016); g – Sen *et al.* (2018). SSZ closure data from: a – Petterson & Windley (1985); b – Treloar *et al.* (1996); c – Rolland *et al.* (2000); d – Heuberger *et al.* (2007); e – Ravikant *et al.* (2009); f – Borneman *et al.* (2015); g – Kumar *et al.* (2017); h – Searle & Hacker (2018).

~99 Ma and ~85 Ma. It appears that the KLA has grown continuously through magmatism spanning from ~85 Ma to 40 Ma, with sparse magmatic pulses at ~102–91 Ma (Fig. 17b) to the south of the SSZ. Most importantly, the quiescent period of magmatism in the Karakoram is apparent during ~99–85 Ma, and the lower age limit of this quiescent period matches well with the timing of initiation of the most pronounced magmatic episode at ~85 Ma in the Kohistan–Ladakh block (Fig. 17b).

https://doi.org/10.1017/S0016756819001547 Published online by Cambridge University Press

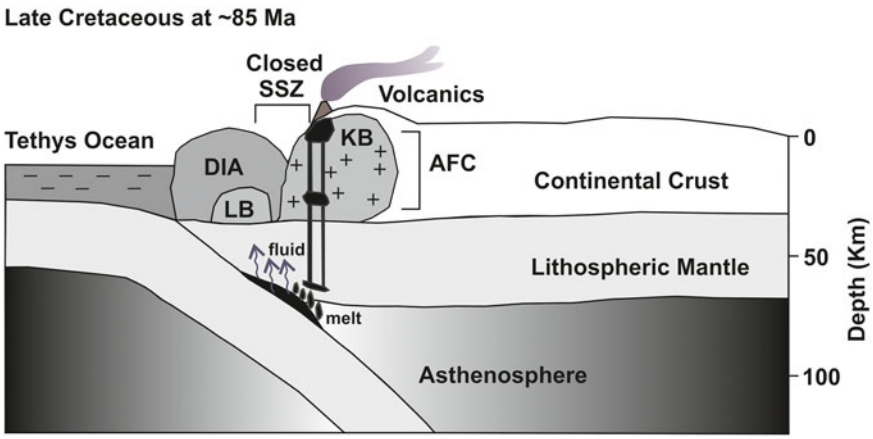

Fig. 18. Configuration of the Shyok suture closure (SSZ) and subsequent collision of the Dras Island Arc (DIA) and Karakoram terrane showing the generation of the Murgo rhyolites at the active continental margin of the Karakoram at ~85 Ma (modified after Jain, 2014; Manikyamba *et al.* 2014). KB – Karakoram Batholith; LB – Ladakh Batholith.

The timing of suturing along the SSZ and collision of the KLA and Karakoram terrane has been suggested as ~110–75 Ma (Petterson & Windley, 1985; Treloar *et al.* 1996; Rolland *et al.* 2000; Heuberger *et al.* 2007; Ravikant *et al.* 2009; Borneman *et al.* 2015; Kumar *et al.* 2017) based on several lines of chronological evidence. These include: (1) ~75 Ma Jutal dykes (Treloar *et al.* 1989) that cross-cut the ~102 Ma Matum das Karakoram pluton and ~113–100 Ma Chalt Volcanics (Petterson & Windley, 1992); (2) an ~85 Ma aplite dyke from the Nubra Valley that cross-cuts the unconformity between the Shyok Volcanics and the Saltoro molasse in the SSZ; (3) ~86–84 Ma granites (Borneman *et al.* 2015) and ~109–104 Ma granites (Kumar *et al.* 2017) that intrude the Shyok Volcanics; (4) a detrital zircon U–Pb age of 92.43 ± 0.24 Ma from the Saltoro molasse that contains zircons from both the Kohistan–Ladakh and Karakoram blocks (Borneman *et al.* 2015).

Extrusive Murgo rhyolite (SM 22) can be seen within the KB and provides a zircon U–Pb age of 84.86 ± 1.87 Ma (Th/U = 0.4–0.8), with some zircon inheritance from Neoproterozoic to Early Cretaceous (782–103 Ma) components (Fig. 13e, f). Interestingly, this sample records the Late Cretaceous event of ~85 Ma (Th/U = 0.7–2.1) (Fig. 13e, f) that is not present in the granites of the KB. We interpret the Late Cretaceous (~85 Ma) age as the eruptive age of the rhyolites, while the observed Early Cretaceous, Neoproterozoic and Late Palaeozoic inherited zircons are xenocrysts most likely entrapped into the melt during the partial assimilation of thickened Karakoram crust formed as a result of the collision of the KLA and Karakoram Block. This proposed model gives an insight into the AFC processes responsible for the evolution of the MV, which possibly originated owing to the partial melting of the mantle wedge, and subsequently experienced AFC at the active continental margin of the Karakoram during the ascent of the magma (Fig. 18).

Based on the above discussion, we suggest that, in the Karakoram terrane, the Albian (~110–100 Ma) was the time period when the eastern and western regions of the KB began evolving owing to the subduction of Tethys oceanic lithosphere along the SSZ. The Karakoram Block then collided with the KLA (Dras island arc) in Late Cretaceous time, before ~85 Ma (Fig. 17). Afterwards, the KLA and Karakoram Block evolved as a single block following the closure of the SSZ in Santonian time, most clearly demonstrated through the observed southward migration of calc-alkaline subduction-related magmatism (Fig. 17b).

Also, the two undeformed granite samples (SM 8 and SM 9A) provide evidence of post-India–Asia collisional magmatic events at ~12 and 15 Ma. Two primary mechanisms are well known for the generation of post-collisional granites in this region. First, the melting of the pelitic source in the upper crust during Miocene time, which is arguably explained by crustal thickening due to the collision of the Indian and Asian plates during Early Eocene time that resulted in this stage of magmatic rocks (Searle *et al.* 1988; Searle, 1991; Fraser *et al.* 2001; Brookfield *et al.* 2017), or second, due to shearing along the lithospheric-scale KF zone (Murphy *et al.* 2000; Weinberg & Dunlap, 2000; Lacassin *et al.* 2004; Valli *et al.* 2008; Leloup *et al.* 2011; Boutonnet *et al.* 2012; Horton & Leech, 2013; Sen *et al.* 2014). In the present case, no deformation related to the KF is seen, and these granites are undeformed (Fig. 3c, d) and lie near to the contact of the SMC and KB. Therefore, we infer the two most plausible models for the generation of post-collisional granite melts. First, these were formed as a result of dehydration melting of a metapelitic source due to high thermal gradients associated with crustal thickening, which served as a significant heat source required for crustal melting (e.g. Parrish & Tirrul, 1989; Schärer *et al.* 1990; Searle *et al.* 2010). Second, these granites represent accumulated melts and were possibly migrated from the pool of magmas formed in batches at depth as a result of shear heating during deformation along the KF.

7. Conclusions

Field, petrographic, geochemical and zircon U–Pb geochronological data from the granites and rhyolites of an unexplored domain of the Karakoram Block exposed along the Shyok Valley have been presented and interpreted, and combined with the previously published zircon U–Pb age data for the magmatic rocks of the Karakoram Block. The main magmatic episode in the Karakoram Block took place during ~110–100 Ma in the western as well as the eastern Karakoram. This study provides a new model for the closure of the SSZ based on the emplacement of calc-alkaline rhyolite that has dominant continental signatures, which most likely resulted from synchronous AFC within the thickened continental margin during the ascent of magma from the mantle wedge. Our results suggest that the closure of the SSZ took place before ~85 Ma. The KLA and the Karakoram Block evolved as a single block after the closure of the SSZ, i.e. after the Late Cretaceous period. After that, the magmatic pulse shifted southwards towards the Ladakh Batholith region, with sparse magmatic events in the Karakoram Block.

Acknowledgements. VA has received funds from the Science and Engineering Research Board grant (EMR/2014/000555) to carry out this work. Authors thank the director, Wadia Institute of Himalayan Geology, Dehradun, for

https://doi.org/10.1017/S0016756819001547 Published online by Cambridge University Press

generous support during present work. Manoranjan Mohanty and Rajwant, DST and SERB, New Delhi thanked for their continuous encouragement. N. K. Juyal thanked for their help during CL imaging, and Chandra Shekhar helped during ICP-MS and XRF analyses. We thank C P. Dorjey, Skalzang Namgyal and Thinless Gyachho for field assistance. We highly acknowledge the Indo-Tibetan Border Police (ITBP) for help and support during fieldwork in the border area of Ladakh Himalaya. We thank two anonymous reviewers and the handling editor Kathryn Goodenough for their constructive and generous scientific comments on the earlier versions of the manuscript that improved the paper substantially.

Supplementary material. To view supplementary material for this article, please visit https://doi.org/10.1017/S0016756819001547

References

Altherr R, Holl A, Hegner E, Langer C and Kreuzer H (2000) High-potassium, calc-alkaline I-type plutonism in the European Variscides: northern Vosges (France) and northern Schwarzwald (Germany). *Lithos* **50**, 51–73.

Bohon W, Hodges KV, Tripathy-Lang A, Arrowsmith JR and Edwards C (2018) Structural relationship between the Karakoram and Longmu Co fault systems, southwestern Tibetan Plateau, revealed by ASTER remote sensing. *Geosphere* **14**, 1837–50.

Borneman NL, Hodges KV, Soest MC, Bohon W, Wartho JA, Cronk SS and Ahmad T (2015) Age and structure of the Shyok suture in the Ladakh region of northwestern India: implications for slip on the Karakoram fault system. *Tectonics* **34**, 2011–33.

Bouilhol P, Jagoutz O, Hanchar JM and Dudas FO (2013) Dating the India–Eurasia collision through arc magmatic records. *Earth and Planetary Science Letters* **366**, 163–75.

Boulin J (1981) Afghanistan structure, Greater India concept and Eastern Tethys evolution. *Tectonophysics* **72**, 261–87.

Boutonnet E, Leloup PH, Arnaud N, Paquette JL, Davis WJ and Hattori K (2012) Synkinematic magmatism, heterogeneous deformation, and progressive strain localization in a strike-slip shear zone: the case of the right-lateral Karakorum fault. *Tectonics* **31**. doi: 10.1029/2011TC003049.

Brookfield ME, Chung SL and Shellnutt JG (2017) Mid-Miocene (post 12 Ma) displacement along the central Karakoram fault zone in the Nubra Valley, Ladakh, India from spot LA-ICPMS U/Pb zircon ages of granites. *Journal of the Geological Society of India* **89**, 231–9.

Chappell BW and White AJR (1974) Two contrasting granite types. *Pacific Geology* **8**, 173–4.

Coward MP, Jan MQ, Rex D, Tarney J, Thirlwall MT and Windley BF (1982) Geo-tectonic framework of the Himalaya of N Pakistan. *Journal of the Geological Society, London* **139**, 299–308.

Coward MP, Rex DC, Khan MA, Windley BF, Broughton RD, Luff IW, Petterson MG and Pudsey CJ (1986) Collision tectonics in the NW Himalayas. In *Collision Tectonics* (eds MP Coward and AC Ries), pp. 203–19. Geological Society of London, Special Publication no. 19.

Cox KG, Bell JD and Pankhurst RJ (1979) *The Interpretation of Igneous Rocks*. London: Allen and Unwin.

Crawford MB and Searle MP (1992) Field relationships and geochemistry of pre-collisional (India-Asia) granitoid magmatism in the central Karakoram, northern Pakistan. *Tectonophysics* **206**, 171–92.

Debon F, Le Fort P, Dautel D, Sonet J and Zimmermann JL (1987) Granites of western Karakorum and northern Kohistan (Pakistan): a composite Mid-Cretaceous to upper Cenozoic magmatism. *Lithos* **20**, 19–40.

Desio A, Tongiorgl E and Ferrara G (1964) On the geological age of some granites of the Karakorum. Hindu Kush and Badakhshan (Central Asia). In *Proceedings of the 22nd International Geological Congress, Delhi, Pt. 11, Sect. 11*, pp. 479–96.

Dunlap WJ and Wysoczanski R (2002) Thermal evidence for early Cretaceous metamorphism in the Shyok suture zone and age of the Khardung volcanic rocks, Ladakh, India. *Journal of Asian Earth Sciences* **20**, 481–90.

Ersoy EY (2013) PETROMODELER (Petrological Modeler): a Microsoft® Excel© spreadsheet program for modelling melting, mixing, crystallization and assimilation processes in magmatic systems. *Turkish Journal of Earth Sciences* **22**, 115–25.

Franz G, Lucassen F, Kramer W, Trumbull RB, Romer RL, Wilke HG, Viramonte JG, Becchio R and Siebel W (2006) Crustal evolution at the Central Andean continental margin: a geochemical record of crustal growth, recycling and destruction. In *The Andes* (eds O Oncken, G Chong, G Franz, P Giese, H-J Götze, VA Ramos, MR Strecker and P Wigger), pp. 45–64. Berlin, Heidelberg: Springer.

Fraser JE, Searle MP, Parrish RR and Noble SR (2001) Chronology of deformation, metamorphism, and magmatism in the southern Karakoram Mountains. *Geological Society of America Bulletin* **113**, 1443–55.

Frost BR, Barnes CG, Collins WJ, Arculus RJ, Ellis DJ and Frost CD (2001) A geochemical classification for granitic rocks. *Journal of Petrology* **42**, 2033–48.

Gergan JT and Pant PC (1983) Geology and stratigraphy of eastern Karakoram, Ladakh. In *Geology of Indus Suture Zone of Ladakh* (eds VC Thakur and KK Sharma), pp. 99–106. Dehra Dun: Wadia Institute of Himalaya Geology.

Hazarika D, Paul A, Wadhawan M, Kumar N, Sen K and Pant CC (2017) Seismotectonics of the Trans-Himalaya, Eastern Ladakh, India: constraints from moment tensor solutions of local earthquake data. *Tectonophysics* **698**, 38–46.

Hazarika D, Sen K and Kumar N (2014) Characterizing the intracrustal low velocity zone beneath northwest India–Asia collision zone. *Geophysical Journal International* **199**, 1338–53.

Heuberger S, Schaltegger U, Burg JP, Villa IM, Frank M, Dawood H, Hussain S and Zanchi A (2007) Age and isotopic constraints on magmatism along the Karakoram-Kohistan Suture Zone, NW Pakistan: evidence for subduction and continued convergence after India-Asia collision. *Swiss Journal of Geosciences* **100**, 85–107.

Hildebrand PR, Searle MP, Khan Z and Van Heijst HJ (2000) Geological evolution of the Hindu Kush, NW Frontier Pakistan: active margin to continent-continent collision zone. In *Tectonics of the Nanga Parbat Syntaxis and the Western Himalaya* (eds M Asif Khan, PJ Treloar, MP Searle and M Qasim Jan), pp. 277–93. Geological Society of London, Special Publication no. 170.

Honegger K, Dietrich V, Frank W, Gansser A, Thöni M and Trommsdorff V (1982) Magmatism and metamorphism in the Ladakh Himalayas (the Indus-Tsangpo suture zone). *Earth and Planetary Science Letters* **60**, 253–92.

Horton F and Leech ML (2013) Age and origin of granites in the Karakoram shear zone and Greater Himalaya sequence, NW India. *Lithosphere* **5**, 300–20.

Hoskin PWO and Schaltegger U (2003) The composition of zircon and igneous and metamorphic petrogenesis. *Reviews in Mineralogy and Geochemistry* **53**, 27–62.

Hu X, Garzanti E, Wang J, Huang W, An W and Webb A (2016) The timing of India-Asia collision onset–facts, theories, controversies. *Earth-Science Reviews* **160**, 264–99.

Jagoutz OE, Burg JP, Hussain S, Dawood H, Pettke T, Iizuka T and Maruyama S (2009) Construction of the granitoid crust of an island arc part I: geochronological and geochemical constraints from the plutonic Kohistan (NW Pakistan). *Contributions to Mineralogy and Petrology* **158**, 739.

Jain AK (2014) When did India–Asia collide and make the Himalaya? *Current Science* **106**, 254–66.

Jain AK and Singh S (2008) Tectonics of the southern Asian Plate margin along the Karakoram Shear Zone: constraints from field observations and U–Pb SHRIMP ages. *Tectonophysics* **451**, 186–205.

Jain AK and Singh S (eds) (2009) *Geology and Tectonics of the South-eastern Ladakh and Karakoram*. Bangalore: Geological Society of India, Publication no. 9.

Janoušek V, Farrow CM and Erban V (2006) Interpretation of whole-rock geochemical data in igneous geochemistry: introducing Geochemical Data Toolkit (GCDkit). *Journal of Petrology* **47**, 1255–9.

Kelemen PB, Shimizu N and Dunn T (1993) Relative depletion of niobium in some arc magmas and the continental crust: partitioning of K, Nb, La and Ce during melt/rock reaction in the upper mantle. *Earth and Planetary Science Letters* **120**, 111–34.

Keppler H (1996) Constraints from partitioning experiments on the composition of subduction-zone fluids. *Nature* **380**, 237.

Khan T, Asif Khan M, Qasim Jan M and Naseem M (1996) Back-arc basin assemblages in Kohistan, Northern Pakistan. *Geodinamica Acta* **9**, 30–40.

Klemperer SL, Kennedy BM, Sastry SR, Makovsky Y, Arinarayana T and Leech ML (2013) Mantle fluids in the Karakoram fault: helium isotope evidence. *Earth and Planetary Science Letters* **366**, 59–70.

Klootwijk CT, Gee JS, Peirce JW, Smith GM and McFadden PL (1992) An early India-Asia contact: paleomagnetic constraints from Ninetyeast Ridge, ODP Leg 121. *Geology* **20**, 395–8.

Krol MA, Zeitler PK and Copeland P (1996) Episodic unroofing of the Kohistan Batholith, Pakistan: implications from K-feldspar thermochronology. *Journal of Geophysical Research: Solid Earth* **101**, 28149–64.

Kumar S (2014) Magmatic processes: review of some concepts and models. In *Modelling of Magmatic and Allied Processes* (eds S Kumar and RN Singh), pp. 1–22. Society of Earth Scientists Series. Switzerland: Springer International Publishing.

Kumar S, Bora S and Sharma UK (2016) Geological appraisal of Ladakh and Tirit granitoids in the Indus-Shyok Suture Zones of Northwest Himalaya, India. *Journal of the Geological Society of India* **87**, 737–46.

Kumar S, Bora S, Sharma UK, Yi K and Kim N (2017) Early Cretaceous subvolcanic calc-alkaline granitoid magmatism in the Nubra-Shyok valley of the Shyok Suture Zone, Ladakh Himalaya, India: evidence from geochemistry and U–Pb SHRIMP zircon geochronology. *Lithos* **277**, 33–50.

Kuritani T, Kitagawa H and Nakamura E (2005) Assimilation and fractional crystallization controlled by transport process of crustal melt: implications from an alkali basalt–dacite suite from Rishiri Volcano, Japan. *Journal of Petrology* **46**, 1421–42.

Lacassin R, Valli F, Arnaud N, Leloup PH, Paquette JL, Haibing L, Tapponnier P, Chevalier ML, Guillot S, Maheo G and Zhiqin X (2004) Large-scale geometry, offset and kinematic evolution of the Karakorum fault, Tibet. *Earth and Planetary Science Letters* **219**, 255–69.

Lallemand S and Heuret A (2017) Subduction zones parameters. In *Reference Module in Earth Systems and Environmental Sciences*, pp. 1–15. Amsterdam: Elsevier. doi: 10.1016/B978-0-12-409548-9.09495-1.

Leloup PH, Boutonnet E, Davis WJ and Hattori K (2011) Long-lasting intracontinental strike-slip faulting: new evidence from the Karakorum shear zone in the Himalayas. *Terra Nova* **23**, 92–9.

Lesher CM, Goodwin AM, Campbell IH and Gorton MP (1986) Trace-element geochemistry of ore-associated and Barren, felsic metavolcanic rocks in the Superior Province, Canada. *Canadian Journal of Earth Sciences* **23**, 222–37.

Maniar PD and Piccoli PM (1989) Tectonic discrimination of granitoids. *Geological Society of America Bulletin* **101**, 635–43.

Manikyamba C, Saha A, Santosh M, Ganguly S, Singh MR, Rao DS and Lingadevaru M (2014) Neoarchaean felsic volcanic rocks from the Shimoga Greenstone Belt, Dharwar Craton, India: geochemical fingerprints of crustal growth at an active continental margin. *Precambrian Research* **252**, 1–21.

Middlemost EA (1994) Naming materials in the magma/igneous rock system. *Earth-Science Reviews* **37**, 215–24.

Mukherjee PK, Singhal S, Adlakha V, Rai SK, Dutt S, Kharya A and Gupta AK (2017) In situ U–Pb zircon micro-geochronology of MCT zone rocks in the Lesser Himalaya using LA-MC-ICPMS technique. *Current Science* **112**, 802–10.

Murphy JB (2006) Igneous rock associations 7. Arc magmatism I: relationship between subduction and magma genesis. *Geoscience Canada* **33**, 145–67.

Murphy MA, Yin A, Kapp P, Harrison TM, Lin D and Jinghui G (2000) Southward propagation of the Karakoram fault system, southwest Tibet: timing and magnitude of slip. *Geology* **28**, 451–4.

Najman Y, Appel E, Boudagher-Fadel M, Bown P, Carter A, Garzanti E, Godin L, Han J, Liebke U, Oliver G and Parrish R (2010) Timing of India-Asia collision: geological, biostratigraphic, and palaeomagnetic constraints. *Journal of Geophysical Research: Solid Earth* **115**. doi: 10.1029/2010JB007673.

Nicolae I and Saccani E (2003) Petrology and geochemistry of the Late Jurassic calc-alkaline series associated to Middle Jurassic ophiolites in the South Apuseni Mountains (Romania). *Swiss Bulletin of Mineralogy and Petrology* **83**, 81–96.

Parrish RR and Tirrul R (1989) U–Pb age of the Baltoro granite, Northwest Himalaya, and implications for monazite U–Pb systematics. *Geology* **17**, 1076–9.

Paton C, Hellstrom J, Paul B, Woodhead J and Hergt J (2011) Iolite: freeware for the visualisation and processing of mass spectrometric data. *Journal of Analytical Atomic Spectrometry* **26**, 2508–18.

Peacock MA (1931) Classification of igneous rock series. *Journal of Geology* **39**, 54–67.

Pearce J (1996) Sources and settings of granitic rocks. *Episodes* **19**, 120–5.

Pearce JA, Harris NB and Tindle AG (1984) Trace element discrimination diagrams for the tectonic interpretation of granitic rocks. *Journal of Petrology* **25**, 956–83.

Peccerillo A and Taylor SR (1976) Geochemistry of Eocene calc-alkaline volcanic rocks from the Kastamonu Area, northern Turkey. *Contributions to Mineralogy and Petrology* **58**, 63–81.

Petterson MG and Windley BF (1985) RbSr dating of the Kohistan arc-batholith in the Trans-Himalaya of north Pakistan, and tectonic implications. *Earth and Planetary Science Letters* **74**, 45–57.

Petterson MG and Windley BF (1992) Field Relations, geochemistry and petrogenesis of the Cretaceous basaltic Jutal Dykes, Kohistan, northern Pakistan. *Journal of the Geological Society, London* **149**, 107–14.

Phillips RJ (2008) Geological map of the Karakoram fault Zone, eastern Karakoram, Ladakh, NW Himalaya. *Journal of Maps* **4**, 21–37.

Phillips RJ, Parrish RR and Searle MP (2004) Age constraints on ductile deformation and long-term slip rates along the Karakoram fault Zone, Ladakh. *Earth and Planetary Science Letters* **226**, 305–19.

Phillips RJ and Searle MP (2007) Macrostructural and microstructural architecture of the Karakoram fault: relationship between magmatism and strike-slip faulting. *Tectonics* **26**. doi: 10.1029/2006TC001946.

Phillips RJ, Searle MP and Parrish RR (2013) The geochemical and temporal evolution of the continental lithosphere and its relationship to continental-scale faulting: the Karakoram Fault, eastern Karakoram, NW Himalayas. *Geochemistry, Geophysics, Geosystems* **14**, 583–603.

Pudsey CJ, Coward MP, Luff IW, Shackleton RM, Windley BF and Jan MQ (1985) Collision zone between the Kohistan arc and the Asian plate in NW Pakistan. *Earth and Environmental Science Transactions of the Royal Society of Edinburgh* **76**, 463–79.

Rai H (1995) Geology of eastern Karakoram, Ladakh District, India. *Nepal Geological Society Journal* **10**, 11–20.

Rao DR and Rai H (2009) Geochemical studies of granitoids from Shyok tectonic zone of Khardung-Panamik Section, Ladakh, India. *Journal of the Geological Society of India* **73**, 553–66.

Ravikant V (2006) Utility of Rb–Sr geochronology in constraining Miocene and Cretaceous events in the eastern Karakoram, Ladakh, India. *Journal of Asian Earth Sciences* **27**, 534–43.

Ravikant V, Wu FY and Ji WQ (2009) Zircon U–Pb and Hf isotopic constraints on petrogenesis of the Cretaceous–Tertiary granites in eastern Karakoram and Ladakh, India. *Lithos* **110**, 153–66.

Reichardt H, Weinberg RF, Andersson UB and Fanning CM (2010) Hybridization of granitic magmas in the source: the origin of the Karakoram Batholith, Ladakh, NW India. *Lithos* **116**, 249–72.

Rex AJ, Searle MP, Tirrul R, Crawford MB, Prior DJ, Rex DC and Barnicoat A (1988) The geochemical and tectonic evolution of the central Karakoram, north Pakistan. *Philosophical Transactions of the Royal Society of London: Series A, Mathematical and Physical Sciences* **326**, 229–55.

Rolland Y, Mahéo G, Pecher A and Villa IM (2009) Syn-kinematic emplacement of the Pangong metamorphic and magmatic complex along the Karakorum Fault (N Ladakh). *Journal of Asian Earth Sciences* **34**, 10–25.

Rolland Y and Pêcher A (2001) The Pangong granulites of the Karakoram fault (western Tibet): vertical extrusion within a lithosphere-scale fault? *Comptes Rendus de l'Académie des Sciences, Series IIA: Earth and Planetary Science* **332**, 363–70.

Rolland Y, Pêcher A and Picard C (2000) Middle Cretaceous back-arc formation and arc evolution along the Asian margin: the Shyok Suture Zone in northern Ladakh (NW Himalaya). *Tectonophysics* **325**, 145–73.

Rowley DB (1996) Age of initiation of collision between India and Asia: a review of stratigraphic data. *Earth and Planetary Science Letters* **145**, 1–13.

https://doi.org/10.1017/S0016756819001547 Published online by Cambridge University Press

Rubatto D and Gebauer D (2000) Use of cathodoluminescence for U–Pb zircon dating by ion microprobe: some examples from the Western Alps. In *Cathodoluminescence in Geosciences* (eds M Pagel, V Barbin, P Blanc and D Ohnenstetter), pp. 373–400. Berlin, Heidelberg: Springer.

Saini NK (1998) A new geochemical reference sample of granite (DG-H) from Dalhousie, Himachal Himalaya. *Journal of the Geological Society of India* **52**, 603–6.

Schaltegger U, Zeilinger G, Frank M and Burg JP (2002) Multiple mantle sources during island arc magmatism: U–Pb and Hf isotopic evidence from the Kohistan arc Complex, Pakistan. *Terra Nova* **14**, 461–8.

Schärer U, Copeland P, Harrison TM and Searle MP (1990) Age, cooling history, and origin of post-collisional leucogranites in the Karakoram Batholith; a multi-system isotope study. *The Journal of Geology* **98**, 233–51.

Schärer U, Xu RH and Allègre CJ (1984) UPb geochronology of Gangdese (Transhimalaya) plutonism in the Lhasa-Xigaze Region, Tibet. *Earth and Planetary Science Letters* **69**, 311–20.

Searle MP (1991) *Geology and Tectonics of the Karakoram Mountains*. Chichester, UK: John Wiley & Sons Incorporated.

Searle MP (2015) Mountain building, tectonic evolution, rheology, and crustal flow in the Himalaya, Karakoram, and Tibet. In *Treatise on Geophysics* (ed. G Shubert), pp. 469–511. Oxford, UK: University of Oxford.

Searle MP, Cooper DJW, Rex AJ and Colchen M (1988) Collision tectonics of the Ladakh-Zanskar Himalaya. *Philosophical Transactions of the Royal Society of London. Series A, Mathematical and Physical Sciences* **326**, 117–50.

Searle MP and Hacker BR (2018) Structural and metamorphic evolution of the Karakoram and Pamir following India–Kohistan–Asia collision. In *Himalayan Tectonics: A Modern Synthesis* (eds PJ Treloar and MP Searle), pp. 555–82. Geological Society of London, Special Publication no. 483.

Searle MP, Parrish RR, Thow AV, Noble SR, Phillips RJ and Waters DJ (2010) Anatomy, age and evolution of a collisional mountain belt: the Baltoro granite batholith and Karakoram Metamorphic complex, Pakistani Karakoram. *Journal of the Geological Society, London* **167**, 183–202.

Searle MP, Parrish RR, Tirrul R and Rex DC (1990) Age of crystallization and cooling of the K2 gneiss in the Baltoro Karakoram. *Journal of the Geological Society, London* **147**, 603–6.

Searle MP and Phillips RJ (2007) Relationships between right-lateral shear along the Karakoram fault and metamorphism, magmatism, exhumation and uplift: evidence from the K2–Gasherbrum–Pangong ranges, north Pakistan and Ladakh. *Journal of the Geological Society, London* **164**, 439–50.

Searle MP, Rex AJ, Tirrul R, Rex DC, Barnicoat A and Windley BF (1989) Metamorphic, magmatic and tectonic evolution of the Central Karakoram in the Biafo-Hushe regions of northern Pakistan. In *Tectonics of the Western Himalayas* (eds LL Malinconico Jr. and RJ Lillie), pp. 47–74. Geological Society of America, Special Paper no. 232.

Searle MP, Weinberg RF and Dunlap WJ (1998) Transpressional tectonics along the Karakoram fault Zone, northern Ladakh: constraints on Tibetan extrusion. In *Continental Transpressional and Transtensional Tectonics* (eds RE Holdsworth, RA Strachan and JF Dewey), pp. 307–26. Geological Society of London, Special Publication no. 135.

Searle MP, Windley BF, Coward MP, Cooper DJ W, Rex AJ, Rex D, Tingdong L, Xuchang X, Jan MQ, Thakur VC and Kumar S (1987) The closing of Tethys and the tectonics of the Himalaya. *Geological Society of America Bulletin* **98**, 678–701.

Sen K, Adlakha V, Singhal S and Chaudhury R (2018) Migmatization and intrusion of "S-type" granites in the trans-Himalayan Ladakh Magmatic Arc of north India and their bearing on Indo-Eurasian collisional tectonics. *Geological Journal* **53**, 1543–56.

Sen K, Mukherjee BK and Collins AS (2014) Interplay of deformation and magmatism in the Pangong Transpression Zone, Eastern Ladakh, India: implications for remobilization of the trans-Himalayan magmatic arc and initiation of the Karakoram Fault. *Journal of Structural Geology* **62**, 13–24.

Shand SJ (1947) *The Eruptive Rocks*. 3rd ed. New York: John Wiley, 444 pp.

Shvolman VA (1978) Relicts of the Mesotethys in the Pamirs. *Himalayan Geology* **8**, 369–78.

Singh S, Kumar R, Barley ME and Jain AK (2007) SHRIMP U–Pb ages and depth of emplacement of Ladakh Batholith, Eastern Ladakh, India. *Journal of Asian Earth Sciences* **30**, 490–503.

Singhal S, Mukherjee PK, Saini NK, Dutt S and Kumar R (2019) Effect of carbon on major element analysis of carbonaceous silicate rocks by WD-XRF: an evaluation of error and its correction. *Geochemistry: Exploration, Environment, Analysis* **19**, 1–38.

Sisson TW and Bacon CR (1999) Gas-driven filter pressing in magmas. *Geology* **27**, 613–16.

Sláma J, Košler J, Condon DJ, Crowley JL, Gerdes A, Hanchar JM., Horstwood MS, Morris GA, Nasdala L, Norberg N and Schaltegger U (2008) Plešovice zircon—a new natural reference material for U–Pb and Hf isotopic microanalysis. *Chemical Geology* **249**, 1–35.

Spandler C, Hermann J, Arculus R and Mavrogenes J (2003) Redistribution of trace elements during prograde metamorphism from lawsonite blueschist to eclogite facies; implications for deep subduction-zone processes. *Contributions to Mineralogy and Petrology* **146**, 205–22.

Srimal N, Basu AR and Kyser TK (1987) Tectonic inferences from oxygen isotopes in volcano-plutonic complexes of the India-Asia Collision Zone, NW India. *Tectonics* **6**, 261–73.

Streule MJ, Phillips RJ, Searle MP, Waters DJ and Horstwood MSA (2009) Evolution and chronology of the Pangong Metamorphic Complex adjacent to the Karakoram fault, Ladakh: constraints from thermobarometry, metamorphic modelling and U–Pb geochronology. *Journal of the Geological Society, London* **166**, 919–32.

Tapponnier P, Mattauer M, Proust F and Cassaigneau C (1981) Mesozoic ophiolites, sutures, and large-scale tectonic movements in Afghanistan. *Earth and Planetary Science Letters* **52**, 355–71.

Taylor SR and McLennan SM (1985) *The Continental Crust: Its Composition and Evolution*. Oxford: Blackwell Scientific Publications, 312 pp.

Thakur VC, Virdhi NS, Rai H and Gupta KR (1981) A note on the geology of Nubra-Shyok area of Ladakh, Kashmir, Himalaya. *Journal of the Geological Society of India* **22**, 46–50.

Thanh NX, Itaya T, Ahmad T, Kojima S, Ohtani T and Ehiro M (2010) Mineral chemistry and K–Ar ages of plutons across the Karakoram fault in the Shyok-Nubra confluence of northern Ladakh Himalaya, India. *Gondwana Research* **17**, 180–8.

Thorpe RS (ed.) (1982) *Andesites: Orogenic Andesites and Related Rocks*. Chichester, UK: Wiley, 724 pp.

Treloar PJ, Petterson MG, Jan MQ and Sullivan MA (1996) A re-evaluation of the stratigraphy and evolution of the Kohistan arc sequence, Pakistan Himalaya: implications for magmatic and tectonic arc-building processes. *Journal of the Geological Society, London* **153**, 681–93.

Treloar P, Rex DC, Coward M P, Petterson MG, Windley BE, Lun IW and Jan MQ (1989) WAr and Ar/Ar geochronology of the Himalayas in NW Pakistan: constraints on the timing of the collision, deformation, metamorphism and uplift. *Tectonics* **8**, 881–909.

Upadhyay R (2008) Implications of U–Pb zircon age of the Tirit granitoids on the closure of the Shyok Suture Zone, northern Ladakh, India. *Current Science* **94**, 1635–40.

Valli F, Leloup PH, Paquette JL, Arnaud N, Li H, Tapponnier P, Lacassin R, Guillot S, Liu D, Deloule E, Xu Z and Mahéo G (2008) New U-Th/Pb constraints on timing of shearing and long-term slip-rate on the Karakorum fault. *Tectonics* **27**. doi: 10.1029/2007TC002184.

van Buer NJ, Jagoutz O, Upadhyay R and Guillong M (2015) Mid-crustal detachment beneath western Tibet exhumed where conjugate Karakoram and Longmu–Gozha Co faults intersect. *Earth and Planetary Science Letters* **413**, 144–57.

Vermeesch P (2018) IsoplotR: a free and open toolbox for geochronology. *Geoscience Frontiers* **9**, 1479–93.

Vogt K, Gerya TV and Castro A (2012) Crustal growth at active continental margins: numerical modeling. *Physics of the Earth and Planetary Interiors* **192**, 1–20.

Wallis D, Phillips RJ and Lloyd GE (2014) Evolution of the eastern Karakoram Metamorphic Complex, Ladakh, NW India, and its relationship to magmatism and regional tectonics. *Tectonophysics* **626**, 41–52.

Weinberg RF and Dunlap WJ (2000) Growth and deformation of the Ladakh Batholith, Northwest Himalayas: implications for timing of continental collision and origin of calc-alkaline batholiths. *The Journal of Geology* **108**, 303–20.

Weinberg RF, Dunlap WJ and Whitehouse M (2000) New field, structural and geochronological data from the Shyok and Nubra Valleys, northern Ladakh: linking Kohistan to Tibet. In *Tectonics of the Nanga Parbat Syntaxis and the Western Himalaya* (eds M Asif Khan, PJ Treloar, MP Searle and M Qasim Jan), pp. 253–75. Geological Society of London, Special Publication no. 170.

Weinberg RF, Mark G and Reichardt H (2009) Magma ponding in the Karakoram Shear Zone, Ladakh, NW India. *Geological Society of America Bulletin* **121**, 278–85.

Weinberg RF and Searle MP (1998) The Pangong Injection complex, Indian Karakoram: a case of pervasive granite flow through hot viscous crust. *Journal of the Geological Society, London* **155**, 883–91.

Whitney DL and Evans BW (2010) Abbreviations for names of rock-forming minerals. *American Mineralogist* **95**, 185–7.

Wiedenbeck MAPC, Alle P, Corfu F, Griffin WL, Meier M, Oberli FV, Quadt AV, Roddick JC and Spiegel W (1995) Three natural zircon standards for U–Th–Pb, Lu–Hf, trace element and REE analyses. *Geostandards Newsletter* **19**, 1–23.

Windley BF (1988) Tectonic framework of the Himalaya, Karakoram and Tibet, and problems of their evolution. *Philosophical Transactions of the Royal Society of London. Series A, Mathematical and Physical Sciences* **326**, 3–16.

Xiao Y, Niu Y, Wang KL, Lee DC and Iizuka Y (2016) Geochemical behaviours of chemical elements during subduction-zone metamorphism and geodynamic significance. *International Geology Review* **58**, 1253–77.

https://doi.org/10.1017/S0016756819001547 Published online by Cambridge University Press